MDPI

Article

Lorentzian Quantum Cosmology from Effective Spin Foams

Bianca Dittrich [1,*] **and José Padua-Argüelles** [1,2,*]

1   Perimeter Institute, 31 Caroline Street North, Waterloo, ON N2L 2Y5, Canada
2   Department of Physics and Astronomy, University of Waterloo, 200 University Avenue West, Waterloo, ON N2L 3G1, Canada
*   Correspondence: bdittrich@perimeterinstitute.ca (B.D.); jpaduaarguelles@perimeterinstitute.ca (J.P.-A.)

Abstract: Effective spin foams provide the most computationally efficient spin foam models yet and are therefore ideally suited for applications, e.g., to quantum cosmology. Here, we provide the first effective spin foam computations of a finite time evolution step in a Lorentzian quantum de Sitter universe. We will consider a setup that computes the no-boundary wave function and a setup describing the transition between two finite scale factors. A key property of spin foams is that they implement discrete spectra for the areas. We therefore study the effects that are induced by the discrete spectra. To perform these computations, we had to identify a technique to deal with highly oscillating and slowly converging or even diverging sums. Here, we illustrate that high-order Shanks transformation works very well and is a promising tool for the evaluation of Lorentzian (gravitational) path integrals and spin foam sums.

Keywords: spin foams; quantum cosmology; quantum gravity

1. Introduction

The real-time or Lorentzian path integral is particularly important for quantum gravity [1–10]. Euclidean quantum gravity approaches rely on a formal Wick rotation to justify a path integral based on the Euclidean gravity action, over Euclidean metrics. However, such Euclidean approaches suffer from the conformal factor problem [11]. Furthermore, the space of Euclidean metrics is quite different from the space of Lorentzian metrics, making the notion of (inverse) Wick rotation in general ill-defined [2–4].

However, the Lorentzian path integral is very challenging to compute. The oscillating amplitude prohibits the application of Monte Carlo methods, and a direct integration or summation typically leads to a very slow convergence. One way to deal with this issue is to deform the integration contour into the complex plane using, e.g., Picard–Lefschetz methods [8,12–23].

In this work, we will consider effective Lorentzian spin foams applied to a cosmological model describing de Sitter space. The spin foam approach [7] provides a path integral for quantum gravity based on the quantum geometric ingredients of loop quantum gravity [24,25]. The derivation of a cosmological dynamics from spin foams is arguably much less developed than loop quantum cosmology [26–29], which studies loop quantum gravity versions of the Wheeler–DeWitt equation. However, there are a number of important open questions in loop quantum cosmology, including whether the theory is fully covariant [30,31] and how loop quantum cosmology relates to the full theory of loop quantum gravity [32,33]. Spin foams can serve as an independent approach to quantum cosmology [34] and might help to answer these questions. However, a key difficulty for spin foams is the extremely high computational demands [35] of models, such as the EPRL/FK model [5,6]. Effective spin foams, introduced in [9,36,37], require far less computational resources. As this paper will illustrate, effective spin foams allow for probing quantum time evolution in cosmology, which, so far, has not been achieved in spin foam cosmology using other spin foam models [34,38–41].

In contrast to previous works on spin foam cosmology [34,38–41], the spin foam partition function discussed in this work will include an unbounded sum over a lapse-like bulk variable. This sum features an oscillating amplitude and is not necessarily absolutely convergent. A key issue that we therefore face here is how to perform this sum. The corresponding path integrals for Regge calculus [23] or for continuum mini-superspace [8] results in proper integrals, and, as mentioned above, can be computed using a deformation of the integration contour in a complexified configuration space or, more specifically, Picard–Lefschetz theory [12–15]. However, these techniques are not applicable to sums.

Here, we will show that one can treat such sums arising from partition functions with oscillating amplitudes with non-linear series transformations [42] and, in particular, Wynn's epsilon algorithm, which accelerates the convergence of these sums. Surprisingly, this technique can also be applied to evaluate expectation values, which involve diverging sums. We identify as a reason for the effectiveness of these techniques the simple asymptotic behavior of the gravitational (Regge) action. This gives hope that these techniques can be applied for more general gravitational and possibly non-gravitational path integrals and sums.

A key question that we will pursue here is how the replacement of integrals into sums affects the dynamics. These sums arise due to (loop) quantum geometry, which prescribes a discrete spectrum for areas [43–45], and it is important to understand how the discreteness of geometric variables such as areas does influence the dynamics.

Effective spin foams [9,36,37] do implement the key principles of spin foam construction, in particular, a discrete area spectrum. They offer two advantages over previous spin foam models [7], which make them particularly suitable for applications to cosmology. The first advantage is that their numerical evaluations are by several magnitudes faster than those for for EPRL/FK models [5,6]. Here, we will provide the first evaluation of cosmological spin foams with an internal bulk (area) variable. One such evaluation on a standard laptop can take less than a second. In contrast, EPRL models require high-performance computational resources and have led to the development of specialized algorithms for their evaluation [35]. Despite these concerted efforts, the most recent works, which evaluate EPRL spin foam amplitudes for cosmology [40,41] via high-performance computation, do not involve a summation over a bulk area variable.[1]

Another important advantage of effective spin foams is that they allow sub-simplices of arbitrary signatures, particularly time-like tetrahedra, triangles, and edges. In contrast, the standard EPRL/FK models rely in their construction on the so-called time gauge, which forces all tetrahedra (and thus triangles and edges) to be space-like. An extension of the EPRL/FK models that includes more general building blocks does exist [43], but the development of numerical techniques for this extended formulation lags very much behind those for the standard formulation [35]. Many cosmological mini-superspace path integrals incorporate an integral over a lapse-like variable (which then might be Wick-rotated). Such a lapse-like variable is difficult to construct if only space-like tetrahedra are allowed.

The effective spin foam models do rely in their construction more directly on the Regge action. The models described here will automatically incorporate the correct (semi-)classical limit. This point has been a major concern for spin foam cosmology [34,38,39] and group field quantum cosmology [46,47]. In our case, the action will have the same critical points (that is, saddle points) as the Regge action, which does, in the appropriate regime, reflect the dynamics of the continuum mini-superspace models. Appropriate regimes, where discretization artifacts can be neglected, have been identified in [48]. The Regge path integral for these cosmological models has been evaluated in [23] and closely reproduced the continuum mini-superspace results [8].

A key difference between effective spin foams and Regge path integral is the implementation of a discrete area spectrum into the former class of models. Here, we will therefore concentrate on the effects induced by this imposition. Our results indicate that

a discrete area spectrum may lead to significant differences for the no-boundary wave functions, affecting the probabilities for the quantum creation of a de Sitter universe.

This paper is organized as follows: We will first provide necessary background on effective spin foams (Section 2.1) and the de Sitter mini-superspace model and its discretization using the so-called ball and shell model (Section 2.2). We will then discuss the issue of configurations with an irregular light cone structure (Section 2.3) and the (cosmological) Regge action (Sections 2.4 and 2.5). Readers familiar with [48] or [23] can skip Sections 2.2–2.5.

We will then provide further necessary ingredients for the construction of the cosmologically effective spin foam model in Sections 2.6 and 2.7. Section 2.8 will summarize the final (ball and shell) models and present the related partition function.

In Section 3, we will provide some background on non-linear sequence transformations, particularly on the higher-order Shanks transform and Wynn's epsilon algorithm.

Wynn's epsilon algorithm is then applied to compute the partition functions and expectation values for the cosmologically effective spin foam models. Section 4.1 will present the results for the cosmological shell model. Here, we will consider the "Lorentzian regime", that is, boundary data that lead to Lorentzian critical points. Section 4.2 will discuss the results for the ball model, where we will consider the "Euclidean regime"—corresponding to boundary data that only have Euclidean (tunneling) saddles. For all cases, we will compare the effective spin foam sum with the Regge path integral and analyze the differences.

We will close with a discussion and outlook on future work in Section 5.

2. The Cosmological Ball and Shell Model with Effective Spin Foams

2.1. Effective Spin Foam Models

Effective spin foam models [9,36,37] are designed to capture key features of the EPRL/FK spin foam models [5,6], but are much more amenable to numerical calculations. We will leverage this fact here and will provide the first evaluation of cosmological spin foam amplitudes that involve the summation over a bulk variable, which can be identified as lapse.

Effective spin foams [7] are defined on triangulations, where all triangles (and possibly all tetrahedra) are decorated with geometric data. The spin foam partition function sums over these geometric data weighted by a model-specific quantum amplitude. All models have in common that this quantum amplitude leads to the Regge action [49], which provides a very elegant discretization of the Einstein–Hilbert action, in the limit of large quantum numbers.

The two key features of spin foams are the following: First, the spectra for geometric operators, such as area operators, are discrete [43–45]. The spin foam partition function sums over geometries, which are characterized by discrete eigenvalues of the area operators associated with the triangles (and, depending on the model, possibly on additional geometric quantities associated with the tetrahedra). For spatial triangles, the spectral gap is characterized by the dimensionless Barbero–Immirzi parameter, whereas the spectral gap for time-like areas is independent of the Barbero–Immirzi parameter.

These discrete spectra lead to the second feature of spin foams [36]: an enlargement of the configuration space of geometries [50–52], which can be effectively described as replacing the length metric by the area metric [53–56]. Spin foam dynamics impose shape matching constraints [57], which suppress fluctuations away from length metric configurations [36,37,58,59]. These constraints are, however, second class and are therefore only imposed weakly, e.g., via Gaussians peaked on configurations that satisfy the constraints. The Barbero–Immirzi parameter also appears here in characterizing the strength of the suppression,[2] e.g., as the variance of the Gaussians [36,52].

As we explain below, due to the symmetry reduction used in the ball and shell models, these shape-matching constraints are automatically satisfied, so this second key feature will not play a role here. The main point of the current article is to understand the effects induced by introducing the discrete area spectra into the model. The summation range

for the bulk area will mostly involve time-like areas. The choice of the Barbero–Immirzi parameter γ will therefore have a very limited influence on the results. We will fix it to $\gamma = 0.1$, as this value has been previously found to lead to a satisfying implementation of the gravitational equation of motion for triangulations consisting of a few building blocks [37].

Whereas the EPRL/FK spin foam amplitudes are defined via a gauge-theoretic reformulation of general relativity [7], the effective spin foam models leverage the Regge action more directly. This can be justified through a higher gauge formulation of gravity [60], which leads to a model directly featuring the Regge action [61,62]. Directly using the Regge action is particularly advantageous if we aim to describe the full Lorentzian spin foam sector. As mentioned above, the original Lorentzian EPRL/FK models only consider space-like sub-simplices, and their extension [43] still faces challenges regarding asymptotics [63] and numerical evaluation [64].

This is another reason why effective spin foam models are much easier to handle and why we are able to implement in this work the first calculation involving a summation over a lapse-like variable.

As we have already mentioned, effective spin foams leverage the Regge action for their construction. This Regge action, however, uses areas as fundamental variables and is therefore known as Area Regge action [65,66]. This Area Regge action does, in principle, lead to different dynamics[3] from the original Length Regge action [49]. This difference, again, plays no role here due to the symmetry restriction we impose. In fact, we will have a one-to-one transformation between the length and area variables in the model. This allows us to easily impose the discrete spectrum conditions for the areas (see Sections 2.4 and 2.6).

Another simplifying construction step that we will take is to work with (Lorentzian) flat building blocks and to implement the cosmological constant via a cosmological constant term in the action. This is again straightforward to perform in effective spin foam models, but has also been used in simplified versions of the EPRL model [38,67]. An alternative procedure is to base the discretization on homogeneously curved building blocks [68–73]. This reduces discretization artifacts [74–76], particularly with regard to the breaking of diffeomorphism symmetry by the discretization [77,78]. The amplitudes of the resulting spin foam models [69–73] are, however, much harder to compute than for the models with flat building blocks, making these models unsuitable for our purposes for now.

2.2. The Discretization

In this work, we aim to construct a numerically accessible model for mini-superspace quantum cosmology, which describes a Lorentzian de Sitter universe.

We will consider a finite time evolution step in a mini-superspace model given by

$$\mathrm{d}s^2 = -N^2(t)\mathrm{d}t^2 + a^2(t)d\Omega^2 \tag{1}$$

where $d\Omega^2$ is the metric on the unit three-sphere. A given mini-superspace configuration is determined by the scale factor $a(t)$ and the lapse variable $N(t)$ as functions of the time parameter t.

Spin foams rely on a discretization of the underlying space-time manifold into a piecewise (Minkowski-) flat geometry. We choose a discretization that allows us to describe the discrete time evolution of spatial discretized hypersurfaces, which are as homogeneous as possible (see [23,48] for more details).

We will use two models, the so-called ball model and the shell model. Variations of the first model have been used in the context of Euclidean quantum gravity [79–81]; the classical dynamics associated with the shell model are described in [48,82,83]. A recent work [23] constructed the Lorentzian Regge path integral describing one time evolution step based on these models. This work [23] illustrated that this simple approximation already captured the main key features of the continuum mini-superspace evolution, and particularly modeled the no-boundary wave function.

The so-called ball model approximates the first time evolution step of the quantum de Sitter universe by a subdivided regular 4-polytope. The center of the 4-polytope corresponds to the beginning of the universe, where the scale factor is vanishing. The outer boundary of the 4-polytope corresponds to a spatial spherical slice of the de Sitter space-time with a finite scale factor. We will consider regular 4-polytopes, whose (three-dimensional) boundary defines a triangulation. There are three such 4-polytopes, known as 5-cell, 16-cell, and 600-cell. To minimize discretization artifacts [48], we will consider the 600-cell, whose boundary consists of 600 tetrahedra. To implement homogeneity, we choose all edge lengths in this boundary to be the same and refer to the squared edge length in the boundary as s_l.

We subdivide the 600-cell into 600 four-simplices by placing a vertex in the center of the 600-cell and by connecting this central vertex with all the vertices in its boundary. We set again all the lengths of these new edges to be equal. It is, however, more convenient to use as a variable the height square s_h of the four-simplices. For positive s_l and negative s_h, the four-simplices satisfy the Lorentzian generalized triangle inequalities, whereas, for positive s_l and positive s_h, the four-simplices satisfy the Euclidean generalized triangle inequalities. One can understand the height square as a discrete analogue of (minus) the squared lapse parameter. For the Regge path integral, considered in [23], one integrates over this variable; for the effective spin foam model, we will replace this integral by a sum.

The shell model describes a time evolution step between two 600-cell boundaries, characterized by the squared edge lengths s_{l_1} and s_{l_1}. Instead of insisting on a triangulation, it is simpler to use as four-dimensional building blocks frusta[4] with a tetrahedral base [82]. We set the length of the edges connecting the two tetrahedra of a given frustum to be equal, but will use, instead of this length, the height square s_h of the frusta as a dynamical variable. This variable can be again understood as an analogue of (minus) the squared lapse variable. In the Regge path integral, we integrate over this variable, and for the effective spin foam model, we sum over this variable.

In summary, the geometry of the spatial hypersurfaces in the ball and shell model is characterized by s_l. By comparing the three-volume of a 600-cell boundary with the three-volume of a three-sphere in the continuum mini-superspace model, we can deduce the following relation between scale factor a and the squared edge length s_l [48] and thus between the scale factor and the area of the triangles in the 600-cell boundary

$$s_l = \nu^2 a^2, \qquad A = \frac{\sqrt{3}}{4} s_l = \frac{\sqrt{3}}{4} \nu^2 a^2, \tag{2}$$

where $\nu \approx 0.654$.

The lapse parameter in (1) is replaced by the squared height s_h. This squared height can also be translated into the area square $\mathbb{A}_{\text{blk}}^{\text{Ball}}$ of the bulk triangles or area square $\mathbb{A}_{\text{blk}}^{\text{Shell}}$ of the bulk trapeziums in the ball and shell model, respectively.

$$\mathbb{A}_{\text{blk}}^{\text{Ball}} = \frac{\sqrt{s_l}}{4\sqrt{2}} \left(s_l + 8 s_h\right), \qquad \mathbb{A}_{\text{blk}}^{\text{Shell}} = \frac{\sqrt{s_{l_1}} + \sqrt{s_{l_2}}}{4\sqrt{2}} \left((\sqrt{s_{l_2}} - \sqrt{s_{l_1}})^2 + 8 s_h \right). \tag{3}$$

Note that these area squares can be negative, null, or positive.

2.3. Regular and Irregular Light Cone Structure

Even though the models we consider are quite simple, they feature configurations with an irregular light cone structure.

In a smooth Lorentzian manifold, a point comes with a regular light cone structure, if, in a small ball around this point, there are exactly two light cones attached to this point. For piecewise Minkowski-flat geometries, which we consider here, one can formulate a set of conditions[5] that ensure a regular light cone structure [23,85,86].

Of particular importance is one such condition, which we will refer to as hinge regularity. Configurations that violate this condition feature imaginary terms in the Regge

action, which comes with a sign ambiguity. This sign ambiguity can be understood as a branch cut for the complexified Regge action [23].

Hinge regularity is particularly important as it is a condition that involves the deficit angles, which are a key ingredient for the Regge action. The deficit angles are attached to the building blocks of co-dimension two, known as hinges. To define the deficit angle, one projects out from all building blocks attached at the hinge the hinge itself. This leads to a two-dimensional piecewise flat manifold given by two-dimensional building blocks b, which all share the vertex v resulting from the hinge. The deficit angle is defined as the difference between the flat angle and the sum of the two-dimensional angles θ_v^b at v in the building blocks b.

If the hinge is time-like, the two-dimensional building blocks b resulting from the projection will all be space-like, and thus, the angles θ_v^b will be Euclidean and the flat angle is given by 2π.

If the hinge is space-like, the two-dimensional building blocks b will be time-like, and we have to deal with Lorentzian angles θ_v^b. These Lorentzian angles, as defined in, e.g., [22,23,87,88], will, in general, include a real part and an imaginary part $\pm \imath k\pi/2$, which comes with a sign ambiguity. Here, k denotes the number of light rays included in the wedge described by θ_v^b. Depending on the sign ambiguity, the Lorentzian flat angle is given by $\pm 2\pi\imath$.

Hinge regularity is violated if the union of the wedges described by θ_v^b does not include exactly four light rays or two light cones. In case of such a violation, the deficit angle includes an imaginary part with a sign ambiguity.

Note that, for hinge regular configurations, the choice of a sign does not affect the deficit angles.

The Regge action [49,87] is given by the sum of the deficit angles weighted by the volume (here area) of the hinges.[6] Hinge regularity violations thus lead to imaginary parts in the Regge action. Depending on the sign of these imaginary parts, these can lead to either a suppression or an enhancement of hinge regularity violating configurations in the path integral.

Both choices of a sign for the Lorentzian action and the Euclidean action arise from a notion of complex Regge action [23]. The sign ambiguity can then be associated with a branch cut, which goes along hinge regularity violating configurations. For the Lorentzian path integral, we then have to decide whether to include such hinge irregular configurations. If we do include such configurations, we have to choose a side for each branch cut.

With the methods presented here, we can consider each of the options. Ref. [23] has, however, found that including irregular configurations for the ball model does lead to a real amplitude, as one also finds in the continuum. We will therefore include irregular configurations and choose the suppressing side, as has also be done in [23]. For some cases, we will provide a comparison with the choice where one does not include the irregular configurations.

As discussed above, the ball model allows us to obtain the no-boundary wave function from the path integral. In [23], the authors showed that choosing the suppressing side of the branch cut will lead to an approximation of the Vilenkin version of the no-boundary wave function. With this choice, we obtain an exponential suppression of the wave function scaling with $\exp(-\frac{c}{\hbar\Lambda})$ (with $c > 0$ a constant factor), as expected from quantum mechanical tunneling. This Vilenkin version of the no-boundary wave function has also been obtained from a Lorentzian mini-superspace model in [8] and a Regge path integral in [23]. The no-boundary wave function from the Regge path integral does approximate the one obtained from the continuum mini-superspace path integral surprisingly well. A key question we will consider here is how the discrete area spectra do the results obtained from the Regge path integral.

Note that one can also choose the enhancing side of the branch cut. This has been done in the recent work [90] in order to compute the entropy for de Sitter space via a simplicial Lorentzian path integral. To obtain the de Sitter entropy, one indeed needs an exponentially

enhanced result scaling with $\exp(+\frac{c}{\hbar\Lambda})$. The corresponding version of the no-boundary wave function is the Hartle–Hawking one.

Although the light cone irregularities and, therefore, the choice of the branch cut side appear to be a discretization artifact, there is a similar ambiguity of integration contour in the continuum, as illustrated by the fact that [91] obtained the Hartle–Hawking version of the no-boundary wave function from a Lorentzian mini-superspace model. The difference between [8] and [91] lies in the choice of how the integration contour navigates an essential singularity in the continuum mini-superspace action at a vanishing lapse. We refer the reader to [90] for a more in-depth discussion of this issue.

2.4. The Regge Action

The effective spin foam models rely on the Regge action [49], which provides a discretization of the Einstein–Hilbert action. This discretization is based on triangulations, and in (length) Regge calculus, one uses lengths attached to the edges of this triangulation as basic variables. In the case of effective spin foams, one instead uses areas as basic variables and, thus, the area Regge action [65,66], which is accompanied by gluing or shape-matching constraints [9,36,57]. However, with the symmetry reduction employed here, we will have the same number of length and area variables, and length and area Regge action will lead to the same equations of motion. That is, as mentioned above, the shape-matching constraints are automatically satisfied.

We can thus start with the length Regge action, which has already been computed for the cosmological model that we will consider here [23,48]. We can then implement a variable transformation to areas, which will allow us to impose that these have a discrete spectrum, as in effective spin foam models.

Using the notation of [23], the Regge action for the ball and shell model has the following form:

$$
\pm\imath\,(8\pi G)S_{\text{Ball}}^{\pm} \;=\; n_e\sqrt{_{\pm}\mathbb{A}_{\text{blk}}}\,\delta_{\text{blk}}^{\pm} + n_t\sqrt{_{\pm}\mathbb{A}_{\text{bdry}}}\,\delta_{\text{bdry}}^{\pm} - \Lambda n_{\tau}\sqrt{_{\pm}\mathbb{V}_{\sigma}}\;,
$$

$$
\pm\imath\,(8\pi G)S_{\text{Shell}}^{\pm} \;=\; n_e\sqrt{_{\pm}\mathbb{A}_{\text{blk}}}\,\delta_{\text{blk}}^{\pm} + n_t\left(\sqrt{_{\pm}\mathbb{A}_{\text{bdry}_1}}\,\delta_{\text{bdry}_1}^{\pm} + \sqrt{_{\pm}\mathbb{A}_{\text{bdry}_2}}\,\delta_{\text{bdry}_2}^{\pm}\right) - \Lambda n_{\tau}\sqrt{_{\pm}\mathbb{V}_{\text{4-frust}}}\;. \qquad (4)
$$

Here, $n_e = 720$, $n_t = 1200$ and $n_{\tau} = 600$ denote the number of edges, triangles, and tetrahedra in the boundary of the 600-cell. (The action does generalize to the 5-cell and 16-cell if one replaces these numbers appropriately.) Note that the number of edges in the boundary of the 600-cell is equal to the number of bulk triangles. We collected the expressions for the complex deficit angles δ_{blk}, the boundary angles δ_{bdry}, the signed area squares $\mathbb{A}_{\text{blk}}$ and $\mathbb{A}_{\text{bdry}}$, and the signed four-volume squares $\mathbb{V}_{\sigma}$ in Appendix A.

In (4), we introduced two different ways of expressing the complex Regge action [23]. These differ in the evaluation of the square root and the logarithm (which appears in the deficit angles $\delta^{\pm}$; see Appendix A) along the principal branch cut, that is, the negative real axis, for these functions. The branch cut values are defined by $\sqrt{_+ -1} = +\imath$, $\sqrt{_- -1} = -\imath$ and $\log_+(-1) = +\imath\pi$, $\log_-(-1) = -\imath\pi$.

The actions S^+ and S^- evaluate the same function for Lorentzian data, which satisfy the hinge regularity condition. This is the case if $s_h < -\frac{1}{8}s_l$ for the ball model and if $s_h < -\frac{1}{8}\left(\sqrt{s_{l_2}} - \sqrt{s_{l_1}}\right)$ for the shell model. Starting from this regular Lorentzian region, we can analytically continue this action[7] to negative values of s_h, which violate these inequalities and describe hinge irregular configurations. As there is a branching point at $s_h = -\frac{1}{8}s_l$ (or $s_h = -\frac{1}{8}\left(\sqrt{s_{l_2}} - \sqrt{s_{l_1}}\right)$ for the shell model), we find different actions when we analytically continue along $s_h = x + \imath\varepsilon$ or $s_h = x - \imath\varepsilon$ with negative x. Going along $s_h = x + \imath\varepsilon$, we find S^+, which, for the hinge-violating configurations, has a negative imaginary term, and going along $s_h = x - \imath\varepsilon$, we find S^-, which, for the hinge-violating configurations, has a positive imaginary term. As in [23], we will work with the choice that suppresses hinge-violating configurations, that is, S^-.

In a Lorentzian (non-degenerate) triangulation, we have $s_h < 0$. This translates into negative or positive bulk area squares. Negative bulk area squares $\mathbb{A}_{\text{blk}} < 0$ describe hinge regular configuration; the null case $\mathbb{A}_{\text{blk}} = 0$ leads to a branching point for the Regge action.

For the ball model, the hinge irregular Lorentzian regime includes bulk areas with $0 < \mathbb{A}_{\text{blk}} < \frac{1}{6}\mathbb{A}_{\text{bdry}}$; for the shell model, the Lorentzian regime extends to $\mathbb{A}_{\text{blk}} < \frac{1}{6}(\sqrt{\mathbb{A}_{\text{bdry}_2}} - \sqrt{\mathbb{A}_{\text{bdry}_1}})^2$. These configurations include a further branching point $\mathbb{A}_{\text{blk}} = \frac{1}{9}\mathbb{A}_{\text{bdry}}$, respectively $\mathbb{A}_{\text{blk}} = \frac{1}{6}(\sqrt{\mathbb{A}_{\text{bdry}_2}} - \sqrt{\mathbb{A}_{\text{bdry}_1}})^2$, where the three-dimensional bulk building blocks are null.

The imaginary parts of S^- are given by

$$
8\pi G\ \text{Im}(S^-_{\text{Ball}}) =
\begin{cases}
n_e 2\pi\sqrt{\mathbb{A}_{\text{blk}}} & \text{for } 0 < \mathbb{A}_{\text{blk}} < \frac{1}{9}\mathbb{A}_{\text{bdry}} \\
-n_e\pi\sqrt{\mathbb{A}_{\text{blk}}} + n_t\pi\sqrt{\mathbb{A}_{\text{bdry}}} & \text{for } \frac{1}{9}\mathbb{A}_{\text{bdry}} < \mathbb{A}_{\text{blk}} < \frac{1}{6}\mathbb{A}_{\text{bdry}}
\end{cases}
,
$$

$$
8\pi G\ \text{Im}(S^-_{\text{Shell}}) =
\begin{cases}
n_e 2\pi\sqrt{\mathbb{A}_{\text{blk}}} & \text{for } 0 < \mathbb{A}_{\text{blk}} < \frac{1}{9}(\sqrt{\mathbb{A}_{\text{bdry}_2}} - \sqrt{\mathbb{A}_{\text{bdry}_1}})^2 \\
-3n_e\pi\sqrt{\mathbb{A}_{\text{blk}}} + n_t\pi(\sqrt{\mathbb{A}_{\text{bdry}_2}} - \sqrt{\mathbb{A}_{\text{bdry}_1}}) & \\
\qquad \text{for } \frac{1}{9}(\sqrt{\mathbb{A}_{\text{bdry}_2}} - \sqrt{\mathbb{A}_{\text{bdry}_1}})^2 < \mathbb{A}_{\text{blk}} < \frac{1}{6}(\sqrt{\mathbb{A}_{\text{bdry}_2}} - \sqrt{\mathbb{A}_{\text{bdry}_1}})^2
\end{cases}
, \quad (5)
$$

and are positive for the entire hinge irregular regime.

The suppressing effect by the imaginary part of the action can be used to avoid summation over the range of values where the imaginary part of the action is very large.

2.5. Critical Points of the Action

The existence of critical points for the action in the ball and shell model has been analyzed in [48]. We will summarize the main points here and will start with the ball model. Here, one does not find a critical point for negative, that is, Lorentzian, values of s_h (or the bulk area) as long as the boundary length square s_l (or $A = \sqrt{\mathbb{A}_{\text{bdry}}}$) is below a certain threshold value s_{thresh1}. Instead, one finds a critical point for positive, that is, Euclidean, values of s_h. This feature mimics the behavior of the mini-superspace model, where one finds Euclidean critical values[8] if the boundary values for the scale factor are both smaller than $a_\Lambda = \sqrt{3/\Lambda}$. In the continuum, the Hamilton–Jacobi function, that is, the action evaluated on the critical points, shows a monotonous behavior. Discretely, this is only the case for $s_l < s_{\text{thresh2}} \approx 1.75/\Lambda$ (for the 600-cell), which translates to a scale factor $a_{\text{thresh2}} \approx \sqrt{4.08/\Lambda}$. We consider the behavior in the regime above this threshold as discretization artifact, and will therefore only consider boundary values below this threshold.

The shell model allows for modeling the behavior of the continuum model, when both boundary scale factors are above the value $a_\Lambda = \sqrt{3/\Lambda}$. One then finds critical points in the Lorentzian regime.[9] For the shell model, we will therefore consider boundary values that lead to Lorentzian critical values.

2.6. Discrete Area Spectra

In (Length) Quantum Regge calculus, the path integral is defined as a continuous integral over the length of the bulk edges of the triangulation. In spin foams, one instead sums over discrete values assigned to the areas of the bulk triangles. These discrete values are determined from the discrete spectra for the loop quantum gravity area operator. For space-like areas (in a space-like tetrahedron), the spectrum is given by [44,45]

$$
\mathbb{A}_{\text{space-like}} = \ell_{\text{P}}^4\gamma^2 j(j+1) \sim \ell_{\text{Planck}}^2\gamma^2 j^2, \quad j = \tfrac{1}{2}, 1, \tfrac{3}{2}, 2, \tfrac{5}{2}\ldots \quad . \tag{6}
$$

Here, $\ell_{\text{P}}^2 = 8\pi G\hbar$ is the Planck length squared and γ is the dimensionless Barbero–Immirzi parameter. We choose this parameter as $\gamma = 0.1$, which is within the range where one can expect the recovery of the Regge equations of motion from spin foams [37]. The spectrum

for the area becomes equidistant for large *j*. For simplicity,[10] we will adopt this equidistant spectrum and include only the integer *j*'s. (The latter corresponds to a definition of loop quantum gravity as an SO(3) gauge theory instead of an SU(2) gauge theory.)

The spectrum for time-like areas is given by [43]

$$\mathbb{A}_{\text{time-like}} = \ell_{\text{Planck}}^4 (n/2)^2, \quad n = 0, 1, 2, 3, \ldots \quad . \tag{7}$$

Thus, the time-like spectrum does *not* depend on the Barbero–Immirzi parameter γ. Similar to the space-like case, we will restrict to $n \in 2\mathbb{N}$.

Adopting these spectra for the area squares of a single triangle (or trapezium) in our symmetry-reduced model will, however, not lead to sensible results. The reason for this is that the change from one spectral value to the next spectral value induces a very large change in the action. That is, the number of spectral values over a few oscillations of the phase of the amplitude $\exp(\iota S)$ is very low, even around the saddle point, and we can therefore not expect a semi-classical regime. See Figure 4 for an example.

This issue is caused by the symmetry reduction. Indeed, assume that we change the area of a bulk triangle by the spectral gap value $(\gamma)\ell_{\text{P}}^2$. Due to our symmetry requirements, the total area will change by $n_e(\gamma)\ell_{\text{P}}^2$, with $n_e = 720$, leading to a rather large change in the action.

Thus, we adjust the spectrum to the symmetry reduction: we divide the spectral gaps for the bulk triangles by the number of bulk triangles (or bulk trapeziums) n_e and the spectral gap for the boundary triangles by the number of boundary triangles $n_t = 1200$. Thus, we have for the bulk triangles

$$\mathbb{A}_{\text{space-like,bulk}} = \frac{\ell_{\text{Planck}}^2}{n_e^2} \gamma^2 j^2, \quad j = 1,, 2, \ldots \quad, \qquad \mathbb{A}_{\text{time-like,bulk}} = \frac{\ell_{\text{Planck}}^2}{n_e^2} n^2, \quad n = 1, 2, \ldots \quad . \tag{8}$$

This choice can be justified by the following consideration: Consider homogeneous configurations with sufficiently large areas. Changing the area of *X* of the n_e bulk triangles by the spectral gap value will still give a configuration that is almost homogeneous and whose action can be approximated by assuming a homogeneous configuration with a suitable adjusted area value. With *X* running from 1 to n_e, we obtain that the total area, that is, the sum of all bulk areas, has changed by n_e times the minimal allowed spectral value. To implement that the total area can change by the spectral gap value, we therefore adjust the spectrum of a single bulk triangle (trapezium) by dividing the area spectral gaps by the number of bulk triangles n_e. Similarly, we adjust the spectrum for a single boundary triangle by dividing the area spectral gap by the number of boundary triangles n_t.

Of course, here, we have made many simplifying assumptions. These will have to be confirmed or corrected by future work that will investigate constructions with less symmetry reductions. These new insights might particularly affect the spectrum for the regime where the total area is relatively small.

A similar need for the adjustment of spectral gaps appears also in Loop Quantum Cosmology [92,93], and the task of fully justifying these choices from the full theory is still open [33,94].

To be able to trace back how the results change if we replace the continuous Regge path integral by the effective spin foam sum, we will also consider a further refinement of the area spectra. That is, we divide the spectral gap by a refinement parameter R_{ref} and compare the spin foam sum using the spectrum (8) with the spin foam sum using a refined spectrum and with the Regge path integral or, in other words, the sum with an infinitely refined spectrum.

2.7. The Path Integral Measure

The second ingredient we have to fix is the measure term for the spin foam summation. As we wish to primarily study the difference between doing a (spin foam) summation and doing a (Regge) path integral, we will adopt the measure from the (Regge) path integral [23].

This Regge measure was derived from the continuum path integral constructed in [8] and led to a very good agreement between the Regge path integral and the continuum path integral.

The (dimensionless) measure for the Regge path integral in the ball model is given by [23]

$$\mu_{\text{Ball}}(s_h)\mathbf{d}s_h \quad = \quad \frac{(-1)^{\frac{3}{4}}}{\ell_P}\frac{s_l^{\frac{1}{4}}}{(-s_h)^{\frac{3}{4}}}\mathbf{d}s_h \tag{9}$$

where the integral is over negative s_h (with the integral oriented to go from $s_h = 0$ to $s_h \to -\infty$). Transforming this measure to area variables gives for the ball model

$$\mu^t_{\text{Ball}}(B_t)\mathbf{d}B_t \ = \ \frac{(-1)^{-\frac{1}{4}}}{\ell_P}\frac{4 \times 2^{\frac{1}{4}}B_t}{\left(\frac{\mathbb{A}_{\text{bdry}}}{3} + 2B_t^2\right)^{\frac{3}{4}}}\mathbf{d}B_t \,, \qquad \mu^s_{\text{Ball}}(B_s)\mathbf{d}B_s \ = \ \frac{(-1)^{-\frac{1}{4}}}{\ell_P}\frac{4 \times 2^{\frac{1}{4}}B_s}{\left(\frac{\mathbb{A}_{\text{bdry}}}{3} - 2B_s^2\right)^{\frac{3}{4}}}\mathbf{d}B_s \qquad . \tag{10}$$

Here, we parametrize the time-like range of the bulk area by $-B_t^2 = \mathbb{A}_{\text{blk}}$ and the space-like range of the bulk area by $B_s^2 = \mathbb{A}_{\text{blk}}$ with $B_t, B_s > 0$. For the time-like range, we integrate from $B_t = 0$ to $B_t \to \infty$ and, for the space-like range, from $B_s = 0$ to $B_s = \sqrt{\mathbb{A}_{\text{bdry}}}/\sqrt{6}$.

We define the measure for the shell model by replacing in μ_{Ball} the boundary variable $\mathbb{A}_{\text{bdry}}$ by the average $\mathbb{A}_{\text{bdry}} \to \frac{1}{2}(\mathbb{A}_{\text{bdry}_1} + \mathbb{A}_{\text{bdry}2_2})$.

2.8. The Spin Foam Sum

The final definition of our cosmological spin foam sum for the ball model is as follows:

$$Z_{\text{Ball}}(\mathbb{A}_{\text{bdry}}) \ = \ \frac{\gamma\ell_P^2}{R_{\text{ref}}n_e}\sum_{j_B=1}^{j_B^{\text{max}}}\mu^s_{\text{Ball}}\left(\frac{\gamma\ell_P^2 j_B}{R_{\text{ref}}n_e}\right)\exp\left(\frac{\imath}{\hbar}S_{\text{Ball}}\left(\mathbb{A}_{\text{bdry}}, \left(\frac{\gamma\ell_P^2 j_B}{R_{\text{ref}}n_e}\right)^2\right)\right) \ +$$

$$\frac{\ell_P^2}{R_{\text{ref}}n_e}\sum_{n_B=1}^{\infty}\mu^t_{\text{Ball}}\left(\frac{\ell_P^2 n_B}{R_{\text{ref}}n_e}\right)\exp\left(\frac{\imath}{\hbar}S_{\text{Ball}}\left(\mathbb{A}_{\text{bdry}}, \left(\frac{\ell_P^2 n_B}{R_{\text{ref}}n_e}\right)^2\right)\right) \tag{11}$$

where $j_B^{\text{max}} = \left[\left[\frac{R_{\text{ref}}\sqrt{\mathbb{A}_{\text{bdry}}}}{\sqrt{6}}\frac{n_e}{\gamma}\right]\right]$, and $[[x]]$ defines the integer part of x. We will later use $R_{\text{ref}} = 1$, that is, the spectrum (8), as well as a refinement factor of $R_{\text{ref}} = 10$.

The partition function for the shell is of the same form as (11). However, it now depends on two boundary values $\mathbb{A}_{\text{bdry}_1}$ and $\mathbb{A}_{\text{bdry}_2}$, and one has $j_B^{\text{max}} = \left[\left[\frac{R_{\text{ref}}(\sqrt{\mathbb{A}_{\text{bdry}_2}} - \sqrt{\mathbb{A}_{\text{bdry}_1}})}{\sqrt{6}}\frac{n_e}{\gamma}\right]\right]$.
We will see that the differences between spin foam sum and Regge path integrals will be minimal; hence, we will only consider $R_{\text{ref}} = 1$.

Apart from the partition function, we will compute the expectation value of $\mathbb{A}_{\text{blk}}$. To this end, we insert B_s^2 and $-B_t^2$ into the sum over j_B and n_B, respectively.

The second sum in (11) includes infinitely many terms and is converging only very slowly (see Figure 1). It even diverges if we insert $-B_t^2$ for the computation of expectation values (see Figure 2). However, it turns out that the so-called acceleration techniques for series convergence work very well in this case and allow also the evaluation of (absolutely) diverging sums arising for the computation of expectation values.
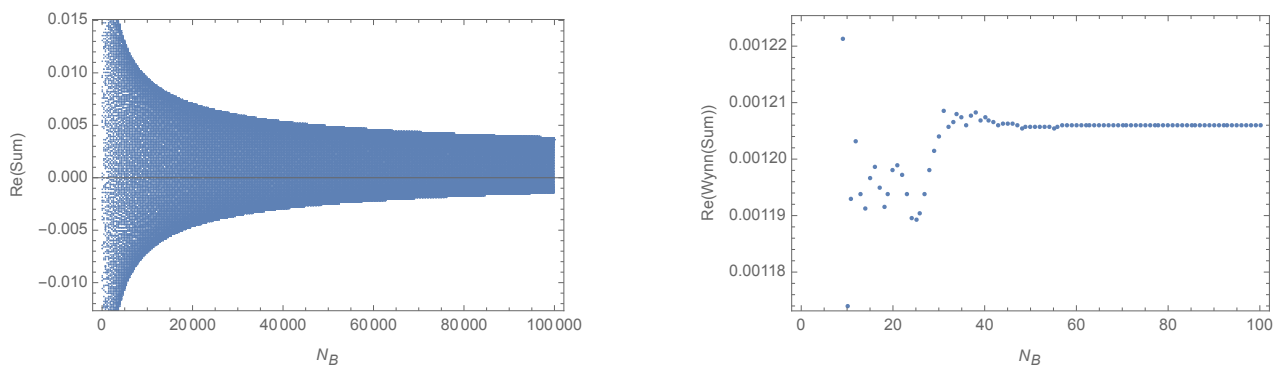
Figure 1. The plot on the left panel shows the partial sums over time-like areas with cut-off N_B for the ball model. We sum all n_B with $n_B \leq N_B$. (The parameters for the spin foam sum area $\Lambda = 0.2\ell_P^{-2}$ and $\sqrt{\mathbb{A}_{\mathrm{bdry}}} \approx 0.033\ell_P^2$.) On the right panel, we show the series resulting from applying Wynn's epsilon algorithm (which will be explained in the main text) to the series defined by the first 100 partial sums shown on the left. The resulting series has a highly accelerated convergence. The maximal relative error (defined in (20)) is of the order of 10^{-11}.
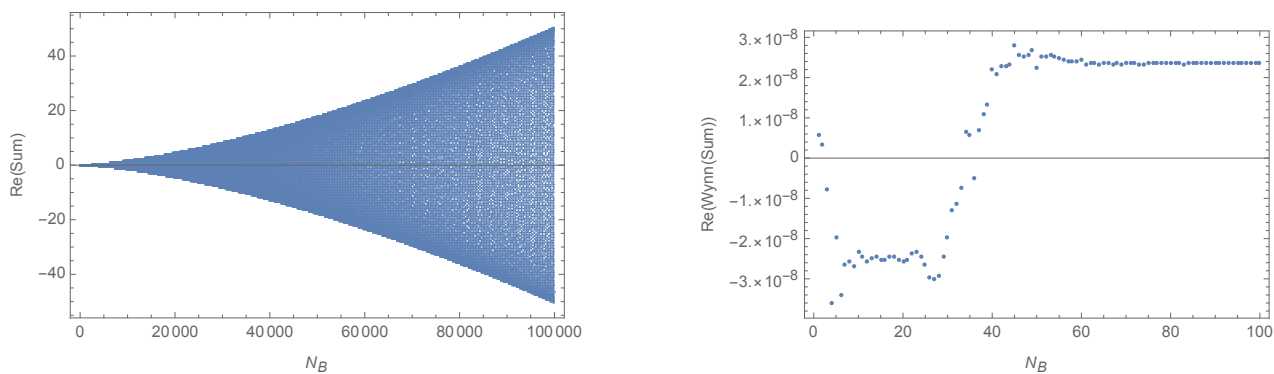
Figure 2. The plot on the left panel shows the partial sums over time-like areas for the computation of the expectation values. That is, compared with the sums shown in Figure 1, we insert a term proportional to n_B^2. As before, we sum over all positive values $n_B \leq N_B$. The right panel shows Wynn's epsilon algorithm applied to the series defined by the first 100 partial sums. This series shows quite a fast convergence. Note that the (anti-) limit is a very small number, which we found is typical for the computation of the expectation values in the ball model. The maximal relative error (defined in (20)) is of the order of 10^{-8}.

3. Acceleration Operators for Series Convergence

As we explained in the previous sections, we have to evaluate oscillating and slowly converging, or even diverging, sums. Direct summation would be very cumbersome; e.g., Figure 1 shows an example for an effective spin foam sum for the ball model. We show the partial sums with up to 10^5 terms, but the result still oscillates with an amplitude that is larger than the absolute value of the limit value. For the evaluation of expectation values, we even encounter diverging sums (see Figure 2). Given that we aim to evaluate a large number of such sums, this process of direct summation is not practical.

Fortunately, there exists a well-developed theory of acceleration operators, also known as non-linear sequence transformations (see e.g., [42]). Such transformations and algorithms are constructed with the aim of accelerating the convergence of slowly converging series, and can also be used to define limit values to divergent series. We will see that these limit values lead to physically reasonable results; e.g., for the computation of expectation values, we rely on such limit values, and in most cases, the expectation values we compute will approximate well the classical solutions.

The non-linear sequence transformations can be applied to compute the limit of sums or integrals with infinite summation or integration range. To treat sums, we form a series from the partial sums $S_k, k = 0, 1, \ldots$

$$S_k = \sum_{n=1}^{C_{\min} + kC_{\text{step}}} f(n) \quad . \tag{12}$$

Here, one can choose an arbitrary minimal cut-off $C_{\min}$ for the sum so that S_0 represents the sum of $C_{\min}$ terms. C_{step} is the step size for probing the partial sums. We found that choosing $C_{\text{step}} = 1$ often leads to the best results.

For the application to integrals, we define

$$S_k = \int_{x_0}^{C_{\min} + k \times C_{\text{step}}} f(x) \, dx \quad . \tag{13}$$

C_{step} should be chosen such that the S_k probes the (largest frequency) oscillations of the integral $S(y) = \int_{x_0}^{y} f(x) dx$; i.e., there should be several S_k for each period.

In the following, we will explain how non-linear sequence transformations can accelerate sequence convergence and briefly sketch the construction of Wynn's epsilon algorithm, which we will use to compute the cosmological Regge path integrals and effective spin foam sums.

3.1. Shanks Transform and Wynn's Epsilon Algorithm

To begin with, we will discuss the Shanks transform. The Shanks transform was derived by Schmidt [95] in 1941 and rediscovered and popularized by Shanks [96] in 1955. To motivate this transform, we consider a model series $\{S_k\}_k$, which we assume to be of the form

$$S_k = S + \alpha t^k \quad . \tag{14}$$

The series converges for $|t| < 1$ to its limit value S. The term αt^k is called a transient. In the case where $|t| > 1$, we have a divergent series. One can nevertheless define S as a limit value (also known as anti-limit) of this series.

Now, if our series $\{S_k\}_{k=1}^{M}$ is (approximately) of the form (14), we can (approximately) determine S from three consecutive values S_k, S_{k+1} and S_{k+2}. Applying (14) to these three values leads to three equations, which can be solved for the three unknowns S, α, and t. The solution for S defines the first-order Shanks transform $\{T_k^1\}_{k=1}^{M-2}$ given by

$$T_k^1 \equiv T^1(S_k, S_{k+1}, S_{k+2}) = S_k - \frac{(S_{k+1} - S_k)^2}{(S_{k+2} - S_{k+1}) - (S_{k+1} - S_k)} \quad . \tag{15}$$

If the original sequence converges, the value of T_k^1 approximates S increasingly better as k is increased (for high enough values) and does so faster than S_k. It is in this sense that convergence has been "accelerated".

In the case where the series $\{S_k\}_k$ has M distinct transients, i.e., is of the form

$$S_k = S + \sum_{m=1}^{M} \alpha_m t_m^k \tag{16}$$

with $1 > |t_1| > |t_2| > \cdots |t_M|$, the first-order Shanks transform eliminates the dominant transient term $\alpha_1 t_1^k$ [42]. This suggests iterating the Shanks transform in order to eliminate all the transients.

An alternative procedure in order to eliminate a larger number of transients from a series, which is (approximately) of the form (16), is to apply an M-th-order Shanks transform. Here, one applies Equation (16) to the $(2M + 1)$ consecutive values $S_k, S_{k+1}, \ldots, S_{k+2M}$

to determine the $(2M + 1)$ unknowns $\{\alpha_m, t_m\}_{m=1}^M$ and S. The solution for S can be via Cramer's rule, expressed via a ratio of determinants (see e.g., [42]). Thus, the M-th-order Shanks transform

$$T_k^M \equiv T^M(S_k, \cdots, S_{k+2M}) \tag{17}$$

returns a series of length $N - 2M$ if the initial series is of the length N. Note that the same holds true for the M-th iteration of the first-order Shanks transform.

Computing determinants is numerically expensive. Fortunately, Wynn's epsilon algorithm allows the computation of the higher-order Shanks transform via a simple recursive scheme. To this end, one defines

$$
\begin{aligned}
\epsilon_k^{(-1)} &= 0, \qquad \epsilon_k^{(0)} = S_k \\
\epsilon_k^{(m+1)} &= \epsilon_{k+1}^{(m-1)} + \frac{1}{\epsilon_{k+1}^{(m)} - \epsilon_k^{(m)}}, \qquad k, m \leq 1 .
\end{aligned} \tag{18}
$$

Wynn [97] could show that the epsilon values with even superscripts ϵ_k^{2m} reproduce the m-th-order Shank transformations

$$\epsilon_k^{(2m)} = T_k^m , \tag{19}$$

whereas the epsilon values with odd superscripts are auxiliary quantities.

Thus, in order to compute a high-order Shanks transform, one can proceed by repeatedly using the second equation in (18), which allows for determining the values $\{\epsilon_k^{(m+1)}\}_{k=1}^{N-2}$ as a function of $\{\epsilon_k^{(m)}\}_{k=1}^{N-1}$ and $\{\epsilon_k^{(m-1)}\}_{k=1}^N$. However, in fact, it is not really necessary to proceed by computing the values $\epsilon_k^{(m)}$ for all k for a fixed m.

It is more efficient [98] to increase k in each iteration step by one, and to compute for each fixed k, the values $\epsilon_{k-m}^{(m)}$. Wynn's moving lozenge technique implements [98] such an iterative scheme (see [42] for a concise description).

This algorithm takes as input a (truncated) series $\{S_k\}_{k=1}^M$ and produces as output $\{T_1^0 = S_1, T_1^1, T_1^2, T_1^3, \ldots, T_1^{[[(M-1)/2]]}\}$ and $\{T_2^0 = S_2, T_2^1, \ldots, T_2^{[[M/2]]-1}\}$. Here, $[[R]]$ denotes the integer part of a real number R. We can summarize both parts into one series $\mathcal{W} \equiv \{S_1, S_2, T_1^1, T_2^1, T_1^2, T_2^2, \ldots, \}$.

Depending on whether M is odd or even, $T_1^{[[(M-1)/2]]}$ respectively $T_2^{[[M/2]]-1}$ should be adopted as the best approximation to the limit value S. Of course, one should choose the parameter M such that the difference between these two values is much smaller than the precision one is interested in.

Wynn's algorithm (18) can lead to a division by very small numbers. This can lead to a termination of the numerical algorithm. One can, however, implement simple stabilization procedures, which prevent a termination of the computation due to overflow caused by this issue [42].

In this work, we will apply Wynn's epsilon algorithm to compute the Regge path integrals and effective spin foam sums. To this end, we have to choose several parameters, i.e., $C_{\min}$ and C_{step} in (12) and (13), as well as the length of the series to which we apply Wynn's epsilon algorithms. The choice of these parameters influences the degree of convergence for the resulting series. To control this rate of convergence, we define the maximal relative error

$$\mathcal{E} = \max_{k \in \mathcal{K}} \frac{|\mathcal{W}_k - \mathcal{W}_{k-1}|}{\frac{1}{2}|\mathcal{W}_k + \mathcal{W}_{k-1}|} , \tag{20}$$

where $\mathcal{K}$ includes the last five labels for the series $\{\mathcal{W}_k\}_k$, which results from Wynn's epsilon algorithm. For computations of the partition functions, we choose the above-mentioned parameters so that $\mathcal{E} < 10^{-6}$. (Often, much smaller maximal errors could be reached,

e.g., $\mathcal{E} < 10^{-12}$). For the computation of expectation values, we encountered a number of examples where it was hard to find parameters that led to such small relative errors. The underlying reason is that the sums for the computation of the expectation values can become very small (see the example in Figure 2). We therefore allowed relative errors of up to $\mathcal{E} < 10^{-3}$.

3.2. Applications

The non-linear sequence transformations, such as the higher-order Shanks transform, are *no*t guaranteed to lead to fast convergence for all series. However, for a series that can be approximated by the form (16), one can expect fast convergence.

In general, we did observe for the examples we computed for this paper a good convergence. We believe that the main reason for this is that the asymptotic behavior of the Regge action for large (time-like) bulk areas is quite simple and particularly linear in the summation/integration variable.[11]

In the case where the action exhibits a saddle point along the Lorentzian integration/summation contour, that is, for our shell model examples, this asymptotic behavior will set in for bulk areas B_t that are only slightly larger than the critical value. In this case, it is advisable to define the partial sums with cut-offs above this critical value. Here, it was generally sufficient to apply Wynn's epsilon algorithm to a series of the length 100 for the spin foam sum (that is, implement a 50th-order Shanks transform) and to a series of the length less than 20 for the Regge integral, for the computation of both the partition functions and expectation values.

In the case where the action does not exhibit saddle points along the Lorentzian integration/summation contour, that is, for our ball model examples, one can also easily identify an asymptotic regime. The resulting sums and integrals tend to lead to numbers much smaller than those in the Lorentzian regime. We therefore experienced more difficulties in obtaining the needed convergence for the computation of the expectation values, particularly for the spin foam sum. For some examples, we had to consider a series of the length 500 to obtain relative maximal errors, which are smaller than 10^{-3}.

The Regge integrals can be computed either by applying Wynn's epsilon algorithm or by using a deformation of the integration contour into the complex plane (see [23]). Naturally, we find in both cases the same results.

The effective spin foam sums cannot be computed via a deformation of the "summation contour". We will comment on this point in more detail in Section 4.2. We therefore have to rely entirely on the method of non-linear sequence transformations. We will see that the spin foam results in the shell model (that is, for examples with saddle points along the integration contour) reproduce very well the Regge integrals and the expectation values closely approximate the classical solutions. This validates the method of non-linear sequence transformation and justifies a posteriori the association of (anti-) limit values with divergent series, which appear for the computation of expectation values.

We note that the first-order Shanks transform agrees with Aitken's delta-squared process [99]. The latter has been applied previously in spin foams [35,100]. The aim there was to provide bounds for the results of an amplitude evaluation involving a cut-off. Numerical constraints allowed only a cut-off on the order of 10^1, and the spin foam evaluation in question led to a non-oscillating series, truncated to an order of 10^1 terms, which appears to converge extremely quickly if compared with Figure 1.

4. Results

4.1. The Shell Model—Examples with a Lorentzian Saddle Point

Here, we will consider the shell model and a range of examples that have one saddle point along Lorentzian data.

Regarding the numerical procedure, these examples with a saddle point along the original integration contour are typically easier to handle than the ball model examples where the saddle point is rather in the complex plane. One obtains fast convergence for,

e.g., Wynn's epsilon procedure, if the minimal cut-off for the lapse variable is chosen such that it includes the saddle point. Beyond the saddle point, the action does go over into a simple asymptotic behavior, which is linear in our summation variable (see Figure 3).
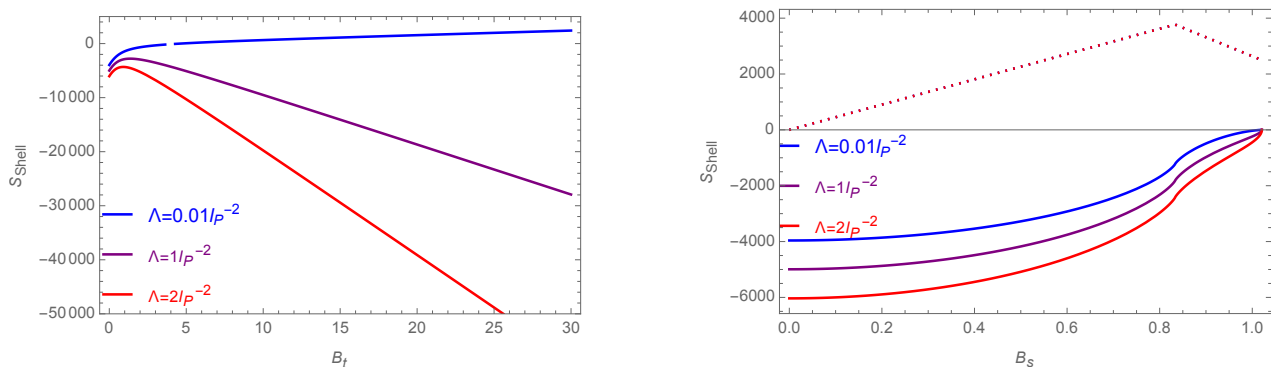
Figure 3. The **left** and **right** panel show the action (in units of ℓ_P^2) as a function of the time-like bulk area B_t (**left panel**) and of the space-like bulk area B_s (**right panel**); both areas are given in terms of ℓ_P^2. Different colors for the graph encode different values for the cosmological constant. We fixed as values for the boundary areas $A_1 = 5\ell_P^2$ and $A_2 = 7.5\ell_P^2$. For space-like areas, the action has a real part (solid lines) and an imaginary part (dashed line). This imaginary part does not depend on the cosmological constant and is therefore the same for all shown cases. The case with $\Lambda = 0.01\ell_P^{-2}$ (in blue) does not have a Lorentzian critical point, but it has a Euclidean one. We will discuss examples with Euclidean critical points in the next section.

The results will show the following:

- The difference between including and excluding the hinge irregular region is relatively small; e.g., the absolute values of the differences in the spin foam sum for the first example below are of the order of 10^{-8}; for the second example, 10^{-6}; and for the third example, 10^{-5}. We will show here the version where we include the hinge irregular region into the path integral. There would not be a visible difference in the plots for the alternative choice.
- The difference between Regge path integrals and effective spin foam sums is relatively small (e.g., see Figure 5).
- The expectation value for the bulk area squared is well approximated by its classical value (e.g., see Figure 6).
- Larger deviations can be found for large values of the cosmological constant (see Figures 13 and 14).

We will illustrate these features with a few examples below.

Let us start with our first example. Here, we choose $\Lambda = 0.2\ell_P^{-2}$ and fix as the smaller boundary area $A_1 := \sqrt{\mathbb{A}_{\text{bdry}_1}} = 5\ell_P^2$. For the larger boundary area, we consider a range from $A_2 = 5.5\ell_P^2$ to $A_2 = 8\ell_P^2$. We can translate these boundary areas to the scale factor squared: $a_1^2 \approx 27\ell_P^2$ and $a_2^2 \approx 29.7\ell_P^2, \ldots, 43.2\ell_P^2$. To do so, we equate the three volumes of the hypersurface of the shell model with the three volumes of the hypersurface in the mini-superspace model (see [48]). Note that, in the mini-superspace model, there are Lorentzian solutions for the lapse function, if both boundary values for the scale factor squared are larger than $a_\Lambda^2 = 15\ell_P^2$.

The main difference between the Regge path integral and the effective spin foam sum is that, in the former case, we integrate over the bulk variable, and in the second case, we rather sum over the spectral values (8). We expect to see large differences between the results if, around the classical solution, there are only very few spectral values per oscillation of the amplitude.

Figure 4 shows that this is not the case, and that we can determine very well the saddle point also with the restriction of the bulk variable to its spectral values (8). We indeed find

that the Regge path integral and the effective spin foam sum approximate each other very well (see Figure 5).
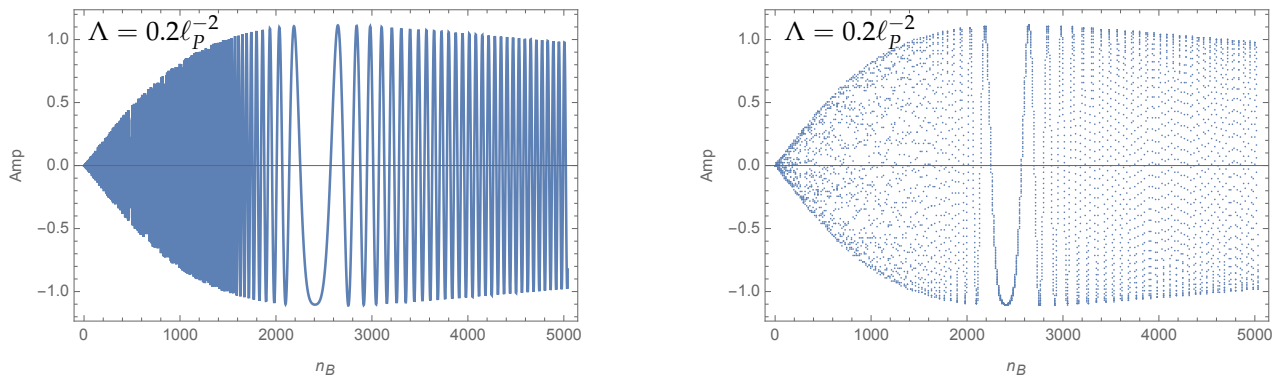

Figure 4. These plots show the amplitude (including the measure term) as a function of the (time-like) summation parameter n_B for the example with $\Lambda = 0.2\ell_P^{-2}$. (That is, $B_t = \ell_P^2 n_B / n_e$ with $n_e = 720$.) On the left panel, we use a continuous plot; on the right panel, we show only the amplitude values for the discrete values of n_B, which we sum over. Note that if we would have used a spectrum $B_t = \ell_P^2 n_B$, the $5040 = 7ne$ points shown on the right panel would reduce to just 7 points.
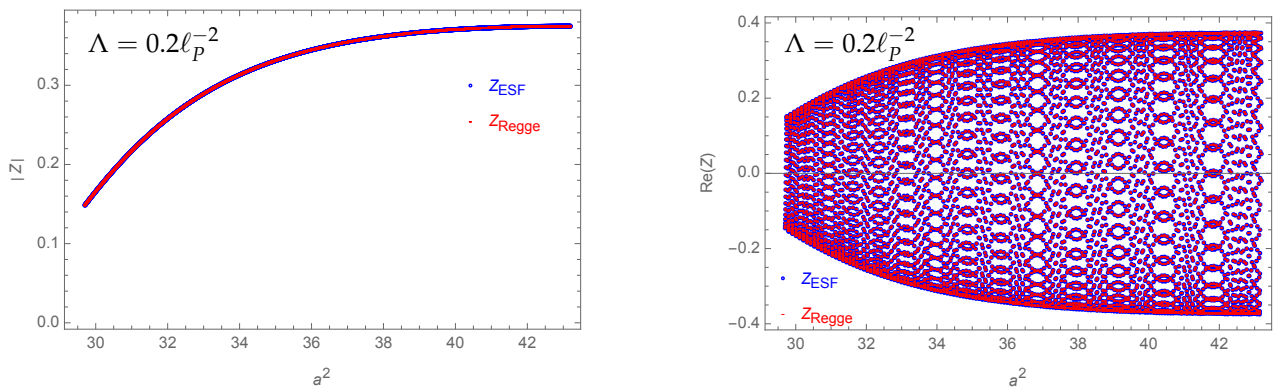
Figure 5. The **left** and **right** panels show the absolute value and the real part of the spin foam sum and Regge integral, respectively. Here, we keep $A_1 = 5.5\ell_P^2$ fixed and vary A_2 from $5.5\ell_P^2$ to $8\ell_P^2$. We translated this boundary area to a scale factor squared according to (2), and express it in units of ℓ_P^2. This applies also to all the following figures. We plotted only every fifth spectral value for the boundary area. For both the absolute value and the real part, differences between spin foam sum and Regge integral are not visible.

Figure 6 compares the (effective spin foam) expectation value of the bulk area squared with the classical solution. The differences for the real part of this expectation values are however not visible in this plot. Tiny oscillations of the expectation value are only visible for larger values of the scale factor if one zooms in (see Figure 7). In Figure 6, we also show the imaginary part of the expectation value. The fact that it does not vanish can be understood as a quantum effect; the ratio of imaginary and real parts is, however, quite small, namely, $\approx 10^{-3}$.
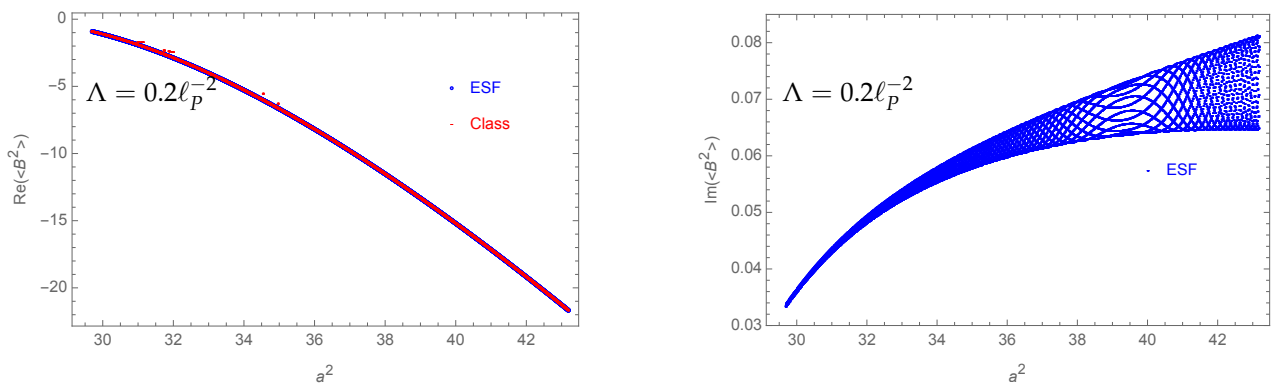
Figure 6. The **left panel** shows the real part of the expectation value of the (signed) squared bulk area $B^2 \equiv \mathbb{A}_{\mathrm{blk}}$ for the spin foam sum and the classical solution. There are no visible differences. The **right panel** shows the imaginary part of the expectation value—the imaginary part of the classical solution is vanishing. Here, we expressed B^2 in units of ℓ_P^4 (also in the following figures).
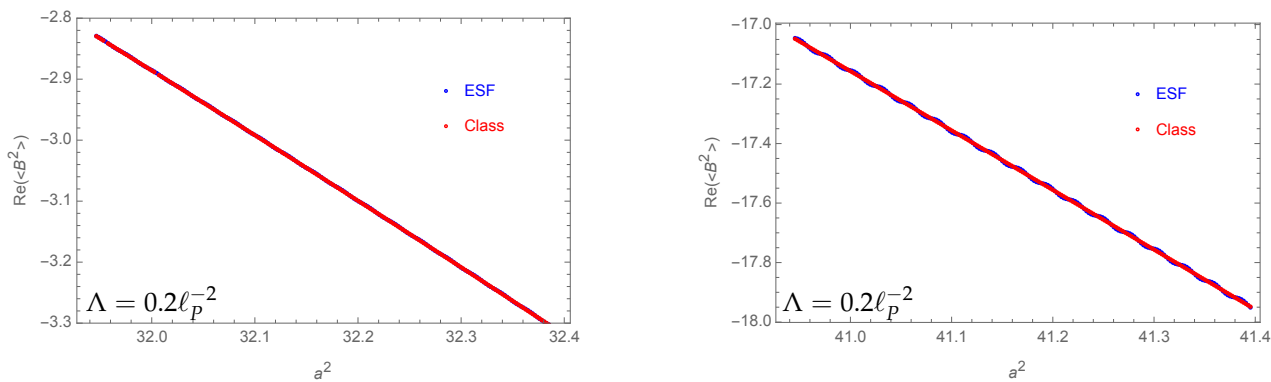

Figure 7. Here, we zoom into a smaller region of the plot shown on the left panel in Figure 6. The left panel shows the expectation value for smaller values of the scale factor squares for the outer boundary a_2^2 (or smaller differences $(a_2 - a_1)^2$) and the right panel for larger differences. In the latter case, we do observe very small oscillations of the expectation value around the classical value.

For the second example, we choose $\Lambda = 2\ell_P^{-2}$. Note that this value is 10 times the value of the cosmological constant in the first example. We choose the boundary areas (or squared scale factors) to be $1/10$ the values in the first example. The actions in the first and second example are then connected by the following scaling behavior

$$S_{\mathrm{Shell}}\left(\frac{1}{c}A_1, \frac{1}{c}A_2, \frac{1}{c}B; c\,\Lambda\right) = \frac{1}{c}\,S_{\mathrm{Shell}}(A_1, A_2, B; \Lambda) \quad . \tag{21}$$

This scaling behavior lets us expect the same number of (bulk area) spectral values per oscillation of the amplitude for examples that are connected by scaling. Indeed, Figure 8 shows that the saddle point is still very well recognizable in this second example, although we show only $1/10$ of the spectral values for the bulk area as compared with the first example.
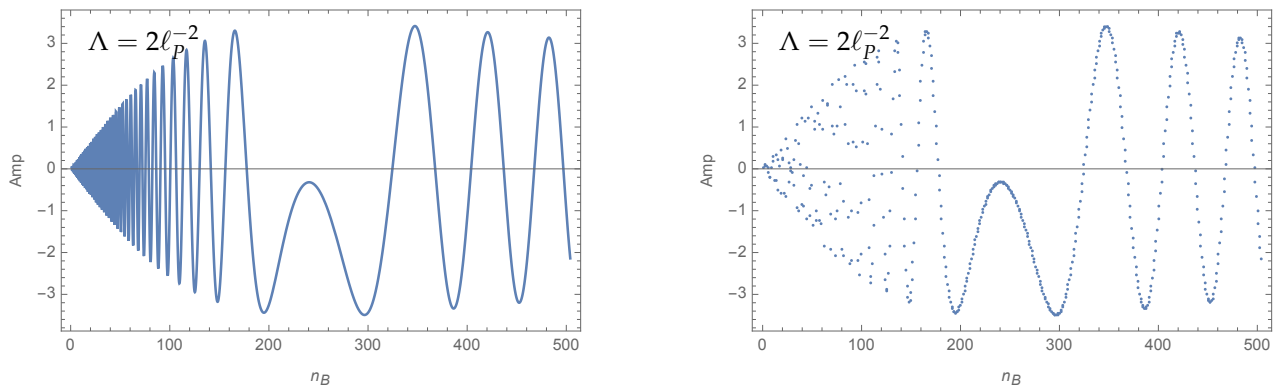
Figure 8. These plots show the amplitude (including the measure term) as a function of the (time-like) summation parameter n_B for the example with $\Lambda = 2\ell_P^{-2}$. This example is connected by scaling (21) to the example shown in Figure 4. Due to this scaling, one has approximately the same number of spectral points per oscillation for the two examples, and could therefore expect the same quality of approximation of the Regge integral by the spin foam sum.

Figure 9 compares the absolute value of the Regge and effective spin foam partition function, and we again see that these approximate each other very well. The real parts of the partition functions differ by a small shift.
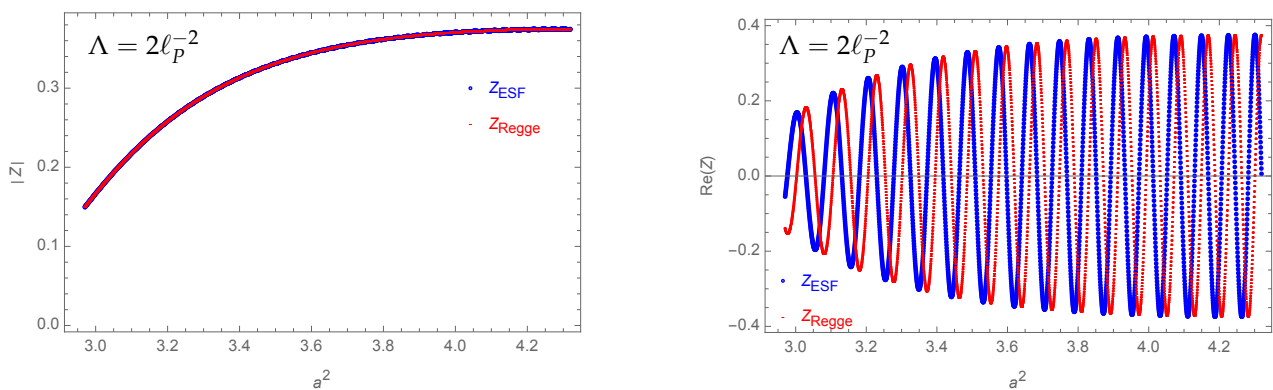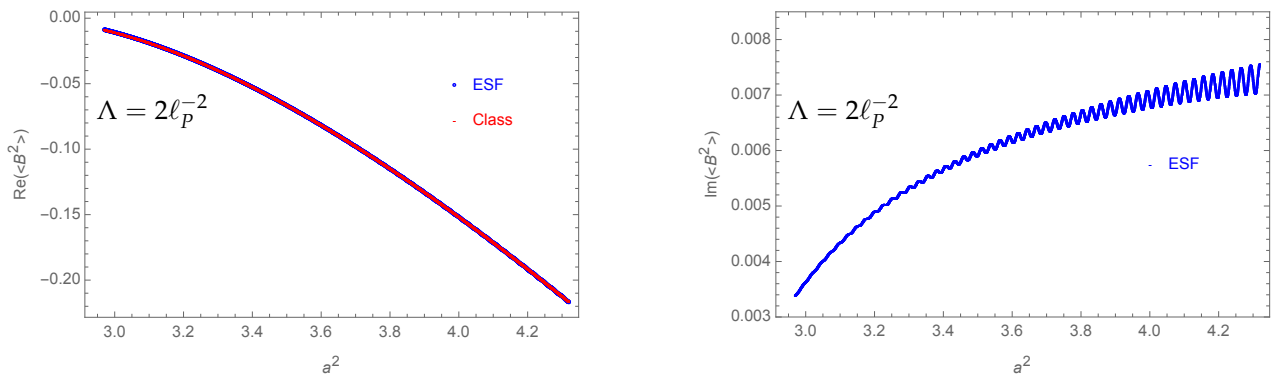

Figure 9. The **left panel** shows the absolute value of the spin foam sum and of the Regge path integral for the second example. The **right panel** shows the real parts. In the latter, we see a small shift in the phase between spin foam sum and Regge path integral. Here, we plot the partition functions for all spectral values in the shown range for the outer boundary area.

We depict the expectation values in Figures 10 and 11. As expected, the real part of the expectation values is connected by the scaling behavior (21). This extends to the size of the imaginary part.

However, zooming in (see Figure 11), we find that the differences between the expectation value and the classical value appear (in their relative size) to be somewhat larger than in the first example, as shown in Figure 7.

We choose the third and last example to showcase an example with larger differences between the Regge and effective spin foam path integral. We found that these differences are enhanced for large values of the cosmological constant and, therefore, choose $\Lambda = 100\ell_P^2$. The boundary values are chosen as $A_1 = 0.2\ell_P^2$ ($a_1^2 \approx 1.1\ell_P^2$) and $A_2 = 0.22\ell_P^2, \ldots, 0.4\ell_P^2$ ($a_1 = 1.2\ell_P^2, \ldots, 2.1$).

Figure 10. The **left panel** shows the real part of the expectation value of the (signed) squared bulk area for the spin foam sum and the classical solution for the second example. There are no visible differences. The **right panel** shows the imaginary part of the expectation value, whose size is approximately 3% of the size of the real part.
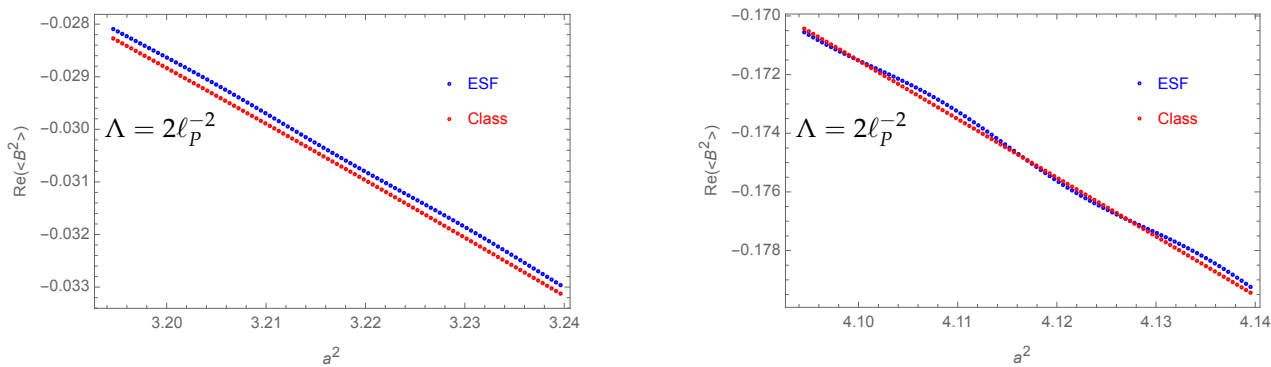

Figure 11. Here, we zoom into the plot shown on the left panel in Figure 10. We see a small shift for smaller values for the outer squared scale factor and small oscillations for larger values for the outer squared scale factor.

Figure 12 shows the amplitude as a function of the continuous bulk variable and as a function of the discrete bulk variable. There is a classical saddle point at $j_B \approx 30$; this classical saddle point is, however, not visible in the discrete plot. We see, however, a so-called pseudo saddle point at $j_B \approx 225$: such saddle points appear if the frequency of the spectral values is similar to the frequency of the oscillations.

One could therefore expect rather large differences between the Regge path integral and the effective spin foam path integral and also large deviations of the effective spin foam results from the classical limit. We will see, however, that the classical results are still reproduced to a surprising degree.

Figure 13 compares the absolute value of the Regge and effective spin foam partition functions. Compared with the previous examples, there are visible differences, which are, however, relatively small. The deviations increase for a growing boundary scale factor a_2^2. This could be due to the fact that there is a pseudo saddle point for larger values of this boundary scale factor, but we could identify no such pseudo saddle point for smaller values of a_2^2.
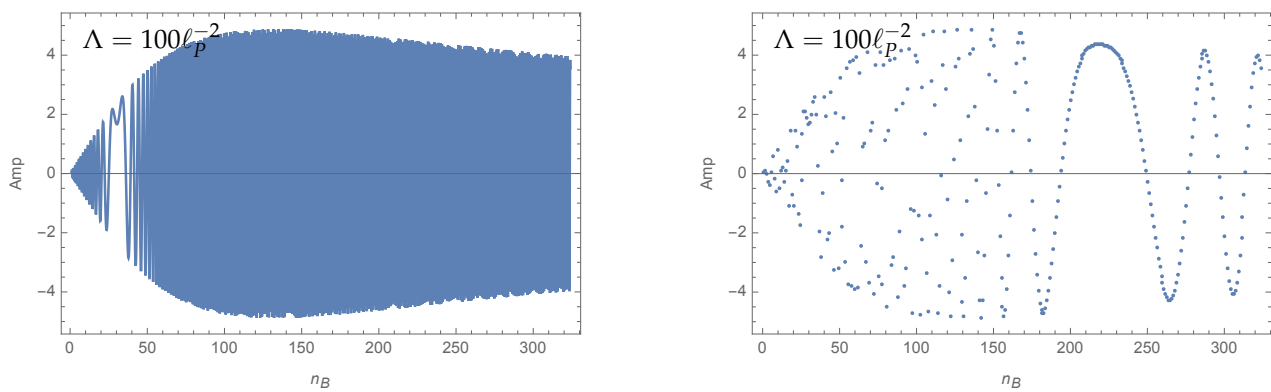
Figure 12. These plots show the amplitude as a function of the (time-like) summation parameter n_B for the example with $\Lambda = 100\ell_P^{-2}$. On the left panel, we show the amplitude as a function of a continuous parameter n_B. Here, we see a (true) saddle point around $n_B = 30$. On the right, we show the amplitude as a function of the discrete summation parameter $n_B \in \mathbb{N}$. Due to the size of the spectral gap, we do not see the (true) saddle point anymore. One rather has a pseudo saddle point around $n_B = 220$, which arises through interference between the discretization and the frequency of the oscillations in the amplitude.
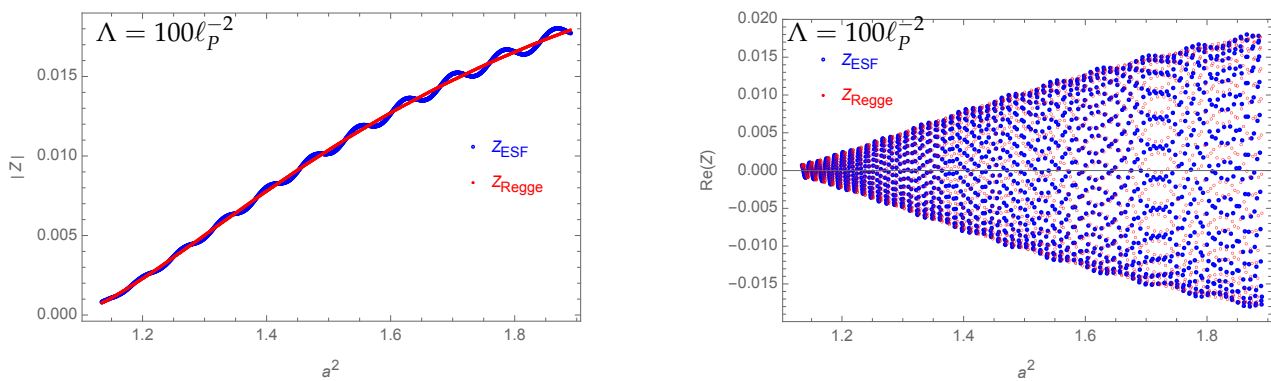

Figure 13. The **left panel** shows the absolute value of the spin foam sum and of the Regge path integral for the third example where $\Lambda = 100\ell_P^2$. The **right panel** shows the real parts. We now do see (small) differences between spin foam sum and Regge integral for both the absolute value and the real part. Here, we again plot the partition functions for every spectral value in the shown range for the outer boundary area.

We compare in Figure 14 the effective spin foam expectation value for the squared bulk area with the classical value. The real part of the expectation value does approximate the classical value quite well, given that we cannot identify the classical saddle point on the right panel of Figure 12. We notice, however, also small oscillations of the expectation value around the classical value, which become more noticeable when we zoom into a smaller range for the boundary scale factor (see Figure 15). The oscillations increase again if we increase the values for a_2^2.

Overall, we find that, for the shell model, with boundary values chosen such that we have classical saddle points for negative values of the bulk area square (and thus satisfying the Lorentzian triangle inequalities), we have relatively small differences between the Regge path integral and the effective spin foam sum on the one hand and the effective spin foam sum expectation value and the classical solution on the other hand.

This does change drastically for examples where we have only a saddle point for a (positive) value of the bulk area square, which satisfies the Euclidean triangle inequalities. Such saddle points can be interpreted to have imaginary lapse and to describe a Euclidean geometry.
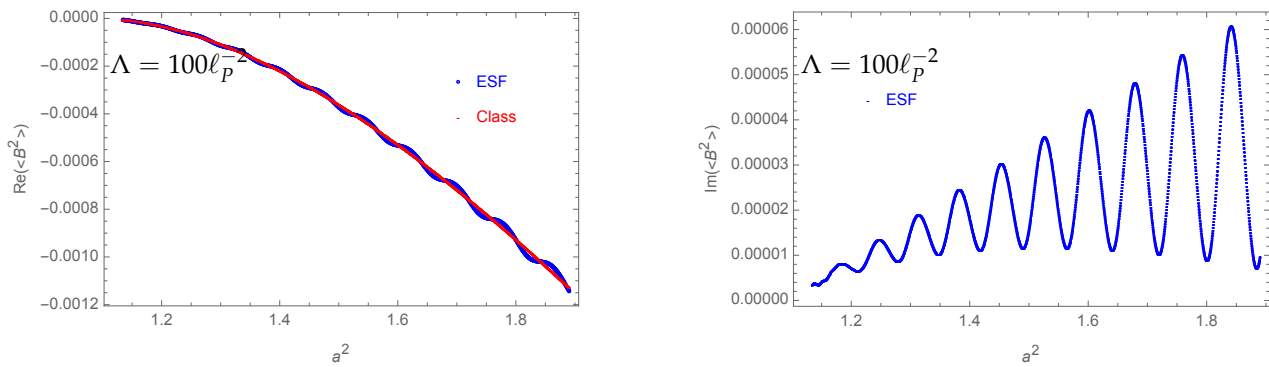
Figure 14. Here, we show real and imaginary parts of the expectation value for the (signed) bulk area squared and compare with the classical solution. The expectation value still approximates the classical value very well, despite the fact that the true saddle point is washed out by the discretization (see Figure 12). We see, however, small deviations with oscillatory behavior.
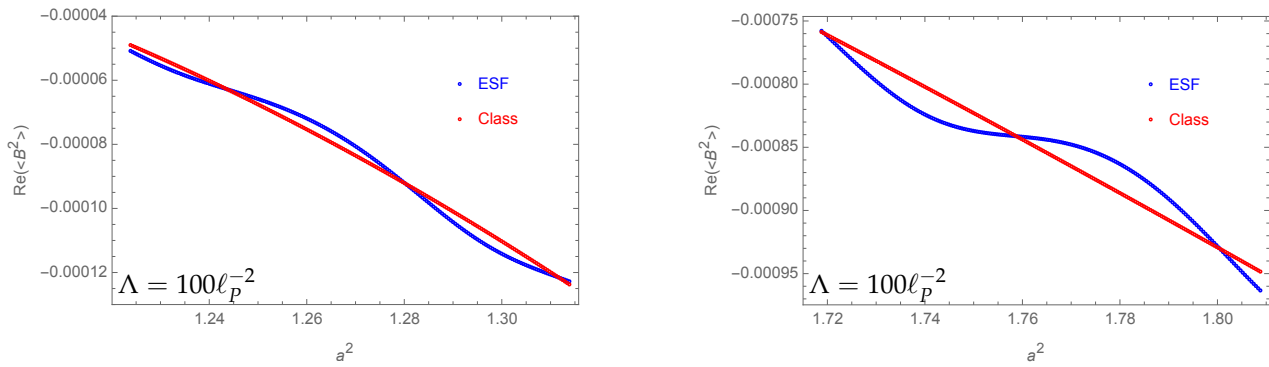
Figure 15. Here, we zoom into the plot shown on the left panel in Figure 14. We now see visible differences between the expectation value and the classical value for both small and larger values of the outer scale factor.

4.2. The Ball Model–Examples with a Euclidean Saddle Point

Here, we will consider the ball model, which implements a boundary value $A_1 = 0$ and thus $a_1^2 = 0$. We will choose the second boundary value that is sufficiently small so that the classical action has a saddle point for a positive bulk area so that Euclidean triangle inequalities are satisfied.

The path integral, as a function of the second boundary value, does the so-called no-boundary wave function [101]. In the continuum mini-superspace model, the path integral can be reduced[12] to a one-dimensional integral over a global lapse parameter. Starting from a Lorentzian contour, one can deform the contour to go along Euclidean data and apply a saddle point approximation [8] or evaluate this integral numerically [23]. In [23], the authors considered the Regge path integral based on the ball model that approximates continuum time evolution with one time step. This reduces the "path integral" to an integral over one variable, which can be interpreted as a lapse. This integral was evaluated using a deformation of the contour to Euclidean data, along which the integral is exponentially decaying. This allowed a numerical integration along this contour. Despite the rather coarse approximation of the continuous time evolution with one simplicial time step, the Regge model provided an astonishingly accurate approximation of the continuum mini-superspace results [23].

Here, we will use, instead of a contour deformation, a direct evaluation of the Lorentzian path integral based on using acceleration operators for series convergence. For the Regge integral, we find exactly the same results as with the contour deformation.

For (effective) spin foams, we replace the integral with a discrete sum, and we thus cannot apply a contour deformation. We will thus rely on the acceleration operator technique. In contrast to the cases with Lorentzian saddle points, we will find for the cases with Euclidean saddle points that the effective spin foam sum substantially deviates from the Regge integral. This deviation grows with the difference between the initial and final scale factors, but appears already for quite small differences. On the other hand, the deviation does decrease if we refine the spectrum for the bulk variable. As one can expect, the deviations vanish when we consider the infinite refinement limit.

We will thus find a drastic difference between the regimes with Lorentzian and Euclidean saddle points. In the cases with Lorentzian saddle points, we found only small differences between the Regge and effective spin foam models, and reproduced the classical expectation value even in cases where the classical saddle points could not be identified in the discrete amplitude plot. That is, the Lorentzian regime is not very sensitive to a discretization of the bulk variable. In contrast, the Euclidean regime appears to be sensitive to such a discretization.

A possible explanation for this sensitivity might be rooted in the fact that, in the Lorentzian regime, the saddle points are on the initial integration contour, whereas in the Euclidean regime, there are no saddle points on the initial integration contour.

If we perform the Regge integral for the examples in the Euclidean regime along the initial contour, the result relies on subtle cancellations between different parts of the amplitude, occurring across the entire integration range. This leads to an overall exponential suppression, which (for larger differences between initial and final scale factors) can lead to very small absolute values for the result of the integral, e.g., on the order of 10^{-6}. These subtle cancellations are easily disturbed by a discretization of the bulk variable. Indeed, we will see that, whereas cancellations still occur in the discrete case, the suppression effect works only to a certain degree, and one will not reach such small numbers as for the continuous integral.

On the other hand, if we do a deformation of the integration contour to Euclidean data, we rely on an analytical continuation. The concept of harmonic functions and analytical continuation can be extended to functions of discrete variables [102]. Such discrete analytical continuations, however, behave quite differently than their continuum counterparts. For example, whereas the analytical continuation of $\exp(\iota x)$ into the upper complex half-plane leads to a decaying function, this is generally[13] not the case for the discrete version of this function.

In view of this discussion, we conjecture that integrals with no saddle points along the initial contour are quite sensitive to a discretization of the integration variable. That is, phenomena like tunneling can be affected. Interestingly, we find that the probability for tunneling tends to increase.

Although we provide a general reason for the deviation between the Regge and effective spin foam model in the Euclidean regime, we want to point out two caveats that will be addressed in future work: the first one is that the results depend on the density of the spectrum of the integration variable. In Section 2.6, we provided a heuristic reasoning for our particular choice in this simplicial mini-superspace model. It would be highly desirable to derive such a spectrum more directly from the non-symmetry reduced theory. This task can be compared with the still-open question to derive loop quantum cosmology more properly from the full theory [94]. The second caveat is that we consider only one time step in our simplicial model. As we explained above, we find that the one-time-step Regge integral approximates the continuum result to an astonishing degree (see [23]). For the effective spin foam model, we find, however, that the deviations from the Regge integral grow with the difference between the boundary values. This could possibly change if we consider multiple time steps and, ultimately, the continuum limit.

We will now present the numerical results in more detail. To begin with, we consider the difference between the Regge integrals with and without including the region with an irregular light cone structure. Figure 16 compares these two integrals for the case

$\Lambda = 0.2\ell_P^{-2}$. We see that the choice where we do include the irregular region leads to a real result for the path integral, whereas not including the irregular region leads to a non-vanishing imaginary part. The continuum mini-superspace model (which does not feature such an irregular region) does lead to a real result. Furthermore, the path integral, which includes the irregular region, shows an exponential decay as a function of the squared scale factor, similar to the continuum mini-superspace model. In contrast, the choice that excludes the irregular region shows an exponential decay only up to a certain threshold value.
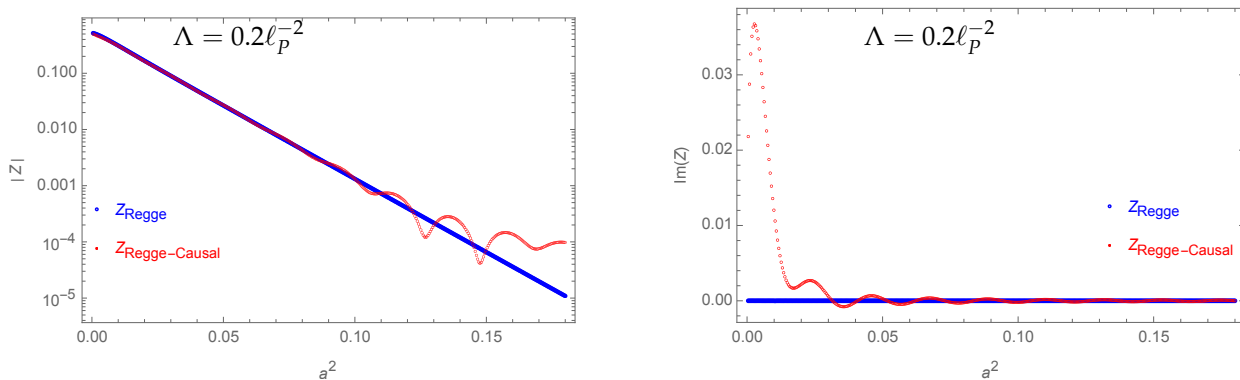

Figure 16. Here, we compare the absolute value (**left panel**, with a logarithmic plot) and imaginary part (**right panel**) of the Regge integral for two different choices: For Z_{Regge}, we integrate over both the hinge regular and irregular configurations; for $Z_{\text{Regge}-\text{Causal}}$, we only integrate over the hinge regular configurations. Including the irregular configurations into the integral leads to a continued exponential decay of the partition function, which is also real. These two features are shared with the path integral for the continuum mini-superspace model.

Thus, if we wish to have a close approximation of the continuum mini-superspace results, we should include the irregular region. In the following, we will only show the choice where we integrate or sum over the irregular region.

For the first example, we will choose $\Lambda = 0.2\ell_P^2$ and $\gamma = 0.1$. For the ball model, the initial boundary area or initial scale factor (squared) is always vanishing. For the final area,[14] we will choose a range from $A = 1 \times (\gamma/n_t)\ell_P^2$, that is, the smallest non-vanish value, to $A = 453 \times (\gamma/n_t)\ell_P^2$. Note that this is only a small part (namely, around 1 %) of the range for the boundary area A that leads to Euclidean saddle points and approximates well the continuum behavior [48]. This regime allows values of up to $A = 45300 \times (\gamma/n_t)\ell_P^2$. However, we will find significant deviations from the Regge path integral already for this small regime.

We will find larger deviations for larger values of the outer area. This can be explained by comparing the spectral gap for the bulk variable with the frequency of the oscillations of the amplitude. Figure 17 shows that this ratio is smaller for larger outer areas. We therefore expect larger deviations in this case.

This is confirmed by comparing the results for the effective spin foam sum with the Regge integral in Figure 18. The (logarithmic) plot for the absolute value of the spin foam sum shows that it deviates from the Regge integral, starting with relative small values for the boundary area, or, equivalently, the squared boundary scale factor. Refining the spectral values for the bulk variable by a factor of 10, one can increase the range where the spin foam sum and Regge integral agree.
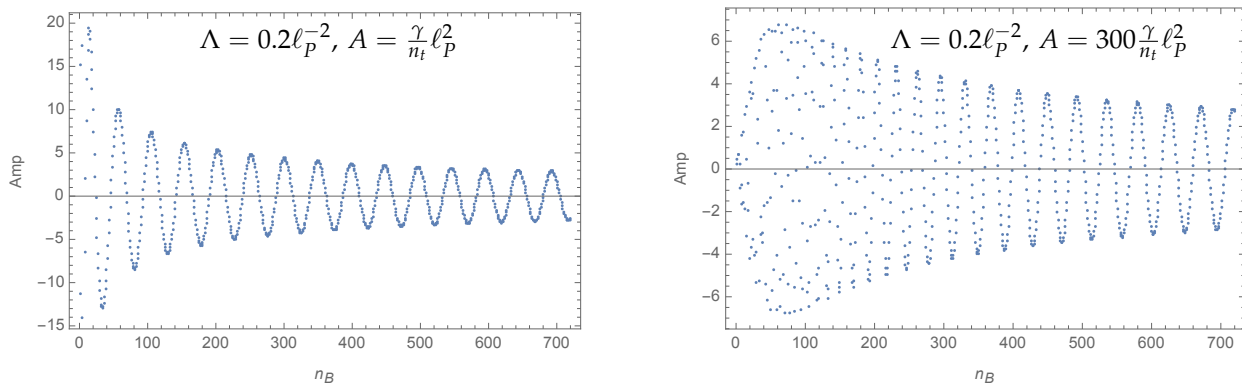
Figure 17. Here, we show the amplitude for a smaller value (**left panel**) and a larger value (**right panel**) of the boundary area A as a function of the discrete (time-like) summation variable n_B. We see that, for larger boundary areas (equivalent to having larger differences between the outer and inner boundary, as the area for the inner boundary is vanishing), the discretization does not fully capture the oscillations of the amplitude over a larger range of the summation variable n_B. One can therefore expect that the difference between Regge integral and spin foam sum is larger for larger outer areas.
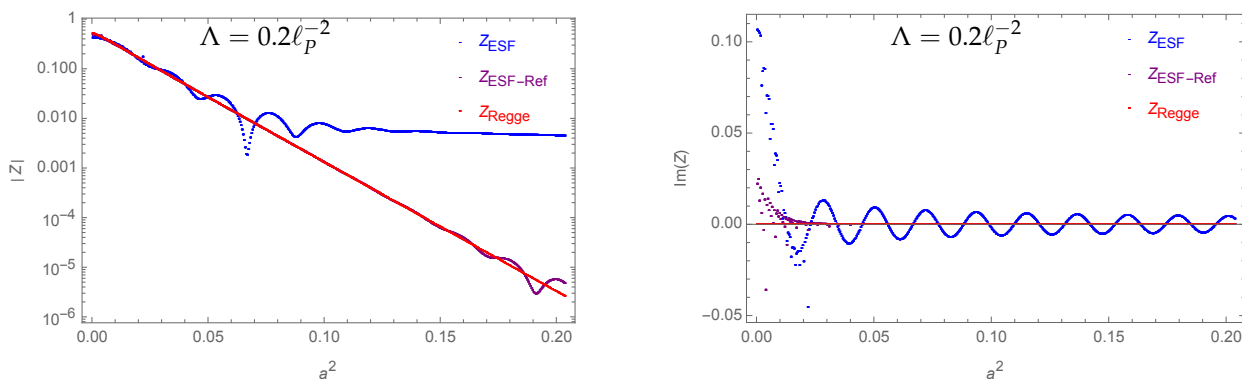
Figure 18. Here, we show the absolute value (with a logarithmic plot on the **left panel**) and the imaginary part (**right panel**) of the partition functions for the ball model. We compare the Regge integral (red) with the effective spin foam sum (blue), with spectral values as described in (8), and the effective spin foam sum (purple), where we refine the spectrum by a factor of 10. We see that the effective spin foam sum does deviate from the Regge path integral for quite small values of the squared scale factor. That is, the discretization (via the discrete spectra) of the integration variable does interfere with the subtle mechanism that leads to destructive interference and an exponential decay of the partition function. Refining the spectrum increases the range for the scale factor, in which the spin foam sum does approximate the Regge integral reasonable well. The imaginary part of the Regge integral does vanish; for the spin foam sums, one does find a non-vanishing imaginary part.

Correspondingly, we find also a non-vanishing imaginary value for the spin foam sum, whereas it does vanish for the Regge integral. The value for the imaginary parts is larger for very small values of the boundary area. However, comparing the size of the imaginary part with the absolute value, we see that the relative size of the imaginary part grows for larger boundary areas and that the amplitude becomes fully oscillatory (see Figure 19).
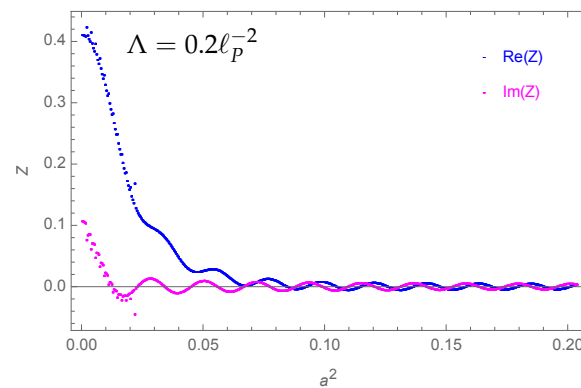
Figure 19. Here, we show real and imaginary parts of the spin foam partition function. The oscillations of the imaginary part are of the same magnitude as the oscillations of the real part, starting with quite small values of the scale factor (squared).

Figure 20 shows the spin foam expectation value for the bulk area squared and compares it with the Regge integral expectation value and the classical[15] value.
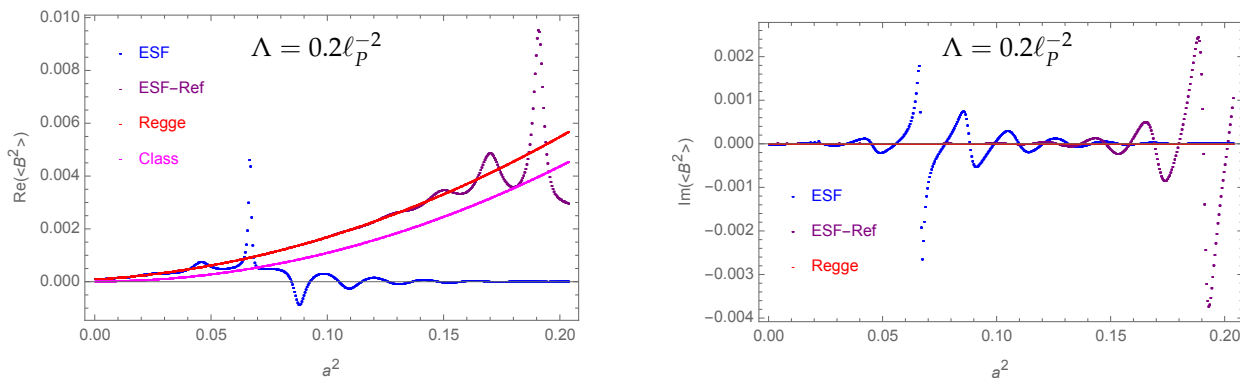

Figure 20. The **left panel** and **right panel** show the real and imaginary parts of the expectation value for the bulk area squared, respectively. We observe that the Regge expectation value already deviates from the critical value of the Euclidean classical action, with the difference increasing with larger scale factors. The effective spin foam expectation value starts to deviate from the Regge expectation value, starting with quite small scale factors. A refinement of the spectrum for the bulk area increases the regime where Regge and (refined) spin foam expectation values coincide.

We see again that the effective spin foam value deviates from the Regge integral value starting with quite small boundary areas. Refining the spectrum (by a factor of 10), we can push the regime where we get agreement between spin foam and Regge result to larger boundary areas. We also find a deviation between the Regge result and the classical value, but they show the same qualitative behavior.

For the second example, we will choose $\Lambda = 2\ell_P^{-2}$. We choose the same range of boundary values for the area as before. Due to having a cosmological constant value that is 10 times the size of the value in the first example, this range now covers 10% (and not only 1%) of the regime in which we approximate well continuum behavior with the Regge path integral.

We noticed that the results for $\Lambda = 2\ell_P^{-2}$ look very similar to the results for $\Lambda = 0.2\ell_P^{-2}$ (for the same range of boundary areas). That is, for these ranges of boundary areas, the value of the cosmological constant has a weak influence. We will therefore just show a comparison of the effective spin foam sums for these two cases in Figure 21.
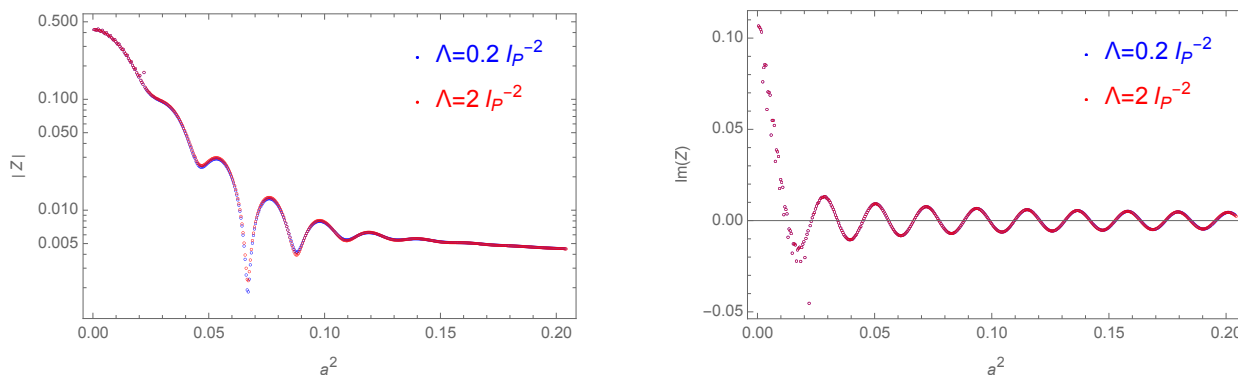
Figure 21. Here, we compare the absolute value of the spin foam partition function (**left panel**, logarithmic plot) and its imaginary part (**right panel**) for the values $\Lambda = 0.2\ell_P^{-2}$ and $\Lambda = 2\ell_P^{-2}$ of the cosmological constant. There are almost no differences visible in this plot.

Increasing the cosmological constant further and further, we decrease the range of boundary values, which lead to an Euclidean saddle point and show for the action evaluated on this saddle point the same qualitative behavior as in the continuum [48]. For example, choosing a value of $\Lambda = 100\ell_P^2$, this range only extends to $A = 90(\gamma/n_t)\ell_P^2$. Here, we find agreement between the effective spin foam and the Regge results (see Figures 22 and 23). However, the reader might want to keep in mind that we are looking at a range of boundary areas, which is five times smaller than in the previous examples, and that we found also agreement in this smaller range in the previous examples.
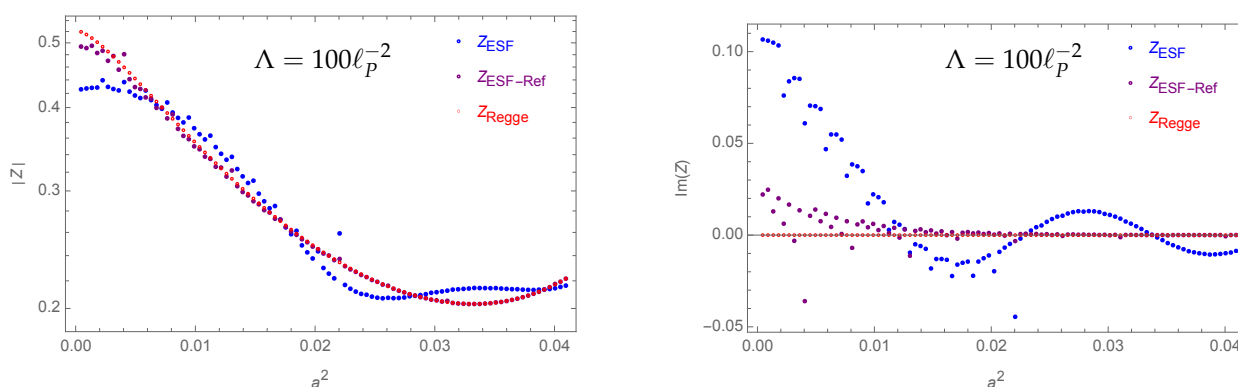
Figure 22. Here, we consider a very large cosmological constant $\Lambda = 100\ell_P^{-2}$ and compare the absolute value (**left panel**, logarithmic plot) and imaginary part (**right panel**) of the partition function for effective spin foams, effective spin foams with refined spectrum, and the Regge integral. We show the entire range of the boundary scale factor squared, for which the classical equations of motions for the discrete model emulate the continuum behavior. This range scales with the inverse of Λ, and is therefore very small, including only 90 eigenvalues for the boundary area. We observe that, over this small range, the differences for the various versions of the partition function are small.

In summary, in the Euclidean regime, we find rather large deviations between the effective spin foam sum and the Regge integral, particularly when comparing with the results in the Lorentzian regime. These deviations grow with the difference between the boundary areas. We still find that the effective spin foam amplitude describing the (tunneling) transition amplitude from a universe with a vanishing scale factor to a universe with a finite scale factor is suppressed. However, above a certain threshold value for the final scale factor, the probability for such transitions is increased in effective spin foams as compared with the Regge path integral.
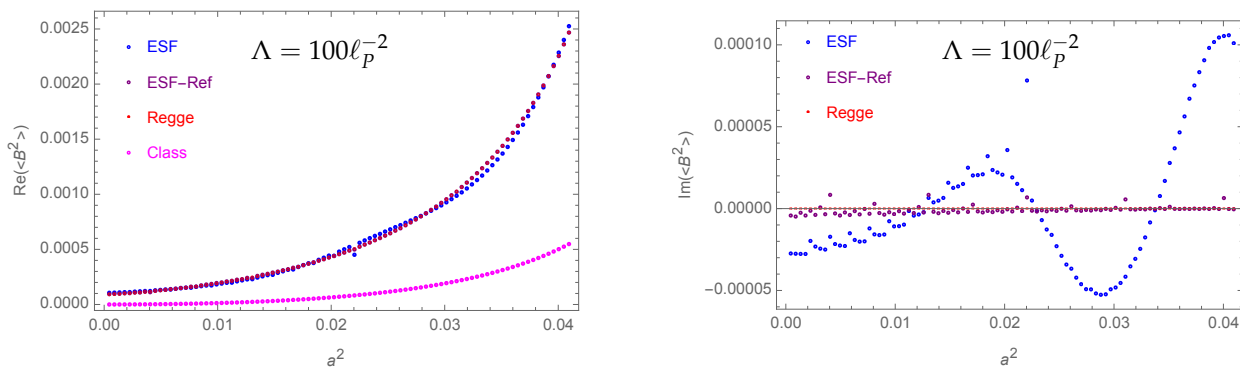
Figure 23. These plots show the real and imaginary part of the expectation value for the bulk area squared, and compare it with the critical value of the classical action. We see that (for the real part) the expectation value for the various versions of partition functions does almost agree, but all deviate from the classical value.

5. Discussion

Here, we discussed a Lorentzian path integral for quantum gravity based on effective spin foams, and applied it to a triangulation modeling homogeneous and isotropic cosmology. Effective spin foams are much more amenable to numerical computations than previous spin foam models and also have no restrictions regarding the space-like or time-like nature of lower-dimensional building blocks. This allowed us to perform the first cosmological spin foam calculations that integrate over a lapse-like bulk variable. One main advantage of this feature is that it allows a direct comparison of the results with the Regge path integral and with quantum mini-superspace cosmology.

The evaluation of Lorentzian path integrals is very challenging due to the oscillating nature of the integrands. We have seen that the integrals and sums we consider are either very slowly converging (Figure 1) or even diverging (Figure 2).

Integrals can be treated by deforming the contour into the complex plane, e.g., following the Picard–Lefschetz prescription [12,13]. We do not have such a technique available for sums, and the theory of discrete harmonic functions does not seem to help. Non-linear transformations of sequences can, however, accelerate the convergence of series very much and may also allow the extraction of (anti-) limits from diverging series [42]. Here, we discovered that the Shanks transforms (and Wynn's epsilon algorithm) are particularly effective in dealing with the series at hand, and that these can be applied to sums and integrals. It also allows the computation of expectation values, which involve divergent series.

The main reason for the effectiveness of these techniques is the simple asymptotic behavior of the Regge action. It seems particularly important that, in the case of the sums, the action is linear in the summation variable [16]. This is the case for the examples considered here but does hold also more generally for spin foams [103,104]. We find it notable that (asymptotically) equidistant area spectra (for $(3 + 1)$ dimensional gravity), as implemented in spin foams, do lead to an action linear in the summation variable, whereas (asymptotically) equidistant length spectra would lead to the problems outlined in Notes[17]. Keeping this lesson in mind, we hope that the Shanks transform and Wynn's epsilon algorithm can be applied to more general gravitational partition functions and more general real-time path integrals.

We have applied the non-linear series transformation to compute the Regge path integral and the effective spin foam sums for two kinds of simplicial min-superspace models, namely, the ball and shell model.

To summarize the results, we first note that the construction of the cosmological effective spin foam models ensures that a saddle point approximation reproduces the correct classical cosmological dynamics, within the regime where discretization artifacts can be neglected [48].[18]

We therefore focused on the transition from the Regge path integral to the effective spin foam sum, that is, the effects induced by implementing the discrete area spectrum. We considered for the shell model boundary conditions that led to critical points along Lorentzian data. We found for this class of examples only small differences between the Regge path integral and the spin foam sum. Indeed, the restriction to Lorentzian critical points means that we have to choose relatively large scale factors: in the continuum, the threshold value is $a_\Lambda = \sqrt{3/\Lambda}$. We did find more significant deviations for a very large cosmological constant $\Lambda = 100\ell_P^2$.

The ball model models a transition from a vanishing scale factor to a finite scale factor and, therefore, implements the no-boundary proposal.[19] The choice of the finite scale factor is restricted to the regime in which the Regge discretization provides a good approximation to the continuum dynamics, which is governed by Euclidean critical points. In a previous work [23], we found that the Regge path integral, in this regime, reproduces very well the continuum mini-superspace results [8], despite the fact that the ball model describes only one time step. In both cases, one finds an exponential decay of the path integral. If one includes hinge irregular configurations into the integral, it does lead to a real partition function, as is also the case in the continuum.

The introduction of the discrete area spectrum (8) does, however, for the choices with a larger finite scale factor, lead to large deviations between the effective spin foam sum and the Regge path integral. The exponential decay (as a function of the outer scale factor) is very much weakened, and the spin foam sum does acquire significant imaginary terms.

We can thus conclude the following: The examples with Lorentzian critical points react fairly insensitively to the introduction of a discrete area spectrum. The examples with Euclidean critical points do lead to significant differences. We provided a heuristic explanation based on the observation that although one can, in principle, apply a deformation of the "integration contour" also for sums, the discrete analytical continuation is much less under control than in the continuum.

The construction of our model did involve a number of simplifications, and lifting these simplifications might affect our conclusions. Future work will address, e.g., the following:

- We provided heuristic arguments for the choice of a discrete area spectrum in (8) in the symmetry-reduced model. A similar issue appears for loop quantum cosmology [94]. It would be desirable to have a more rigorous derivation of the spectrum in symmetry-reduced models. One way to achieve this is to allow for more inhomogeneous bulk variables and to then integrate out the inhomogeneities and, in this way, to define an effective model for only symmetry-reduced configurations, that is, to implement a coarse graining and renormalization process [76,84,108,109].

- We only considered one time step. With the shell model, we can easily incorporate more time steps, in both the Euclidean and Lorentzian regime. We found that, for both the Lorentzian and Euclidean regime, the deviations between Regge integral and spin foam sum got stronger with larger differences between the initial and final scale factor. It will be interesting to see whether we arrive at the same conclusion if we incorporate more time steps, and how, e.g., the threshold value beyond which we see strong deviations in the Euclidean regime changes.

A further advantage of introducing more time steps (and eventually performing the refinement limit) is that the refinement limit can also restore time reparametrization invariance. This has already been demonstrated for the classical dynamics in [48]. We expect that this will also resolve ambiguities for the path integral measure, as has been illustrated in [110–112]. Here, it will be particularly interesting to study the role of the irregular hinge configurations, e.g., whether it will be necessary to include these in order to achieve time reparametrization invariance. With the time reparametrization invariance restored, one can derive a Hamiltonian constraint and the effective spin foam partition function (when defined to include the sum over positive and negative lapse variables) will

satisfy this constraint [110,113,114]. (Note that the ball model does automatically satisfy a so-called post-constraint equation [113,114]).

Other interesting extensions to the model presented here include the addition of matter and the study of the possibility of a singularity resolution. A simple dust action has already been considered in [48,82]. In a similar vein, it will be highly interesting to add more geometric variables that, e.g., describe anisotropies [115].

These efforts will lead to partition functions that involve the summation of several or even many variables. Let us note that, e.g., the Shanks transformation can be generalized to examples with more than one summation variable. One can, e.g., organize the multiple sums into one sequence [116]. A possible organization principle for path integrals is to integrate or sum first over all configurations whose actions evaluate to a value in a certain small range. This seems particularly promising, as the Regge gravitational action shows a simple asymptotic behavior when all bulk areas or edge lengths are scaled large [103,104].

Author Contributions: B.D. and J.P.-A. contributed equally to all aspects of the article. All authors have read and agreed to the published version of the manuscript.

Data Availability Statement: The original contributions presented in the study are included in the article, further inquiries can be directed to the corresponding author/s.

Conflicts of Interest: The authors declare no conflict of interest.

Appendix A. Regge Actions for the Ball and Shell Model

Here, we will provide a more detailed account of the Regge actions for the ball and shell model.

The action for the ball model has the following form:

$$\pm \imath \, (8\pi G) S_{\text{Ball}}^{\pm} \;\; = \;\; n_e \sqrt{{}_{\pm}\mathbb{A}_{\text{blk}}} \, \delta_{\text{blk}}^{\pm} + n_t \sqrt{{}_{\pm}\mathbb{A}_{\text{bdry}}} \, \delta_{\text{bdry}}^{\pm} - \Lambda n_\tau \sqrt{{}_{\pm}\mathbb{V}_\sigma} \quad , \tag{A1}$$

where the various geometric quantities are given by

$$\sqrt{{}_{\pm}\mathbb{A}_{\text{blk}}} \;\; = \;\; \frac{\sqrt{s_l}}{4\sqrt{2}} \sqrt{{}_{\pm} \, s_l + 8 s_h} \quad ,$$

$$\delta_{\text{blk}}^{\pm} \;\; = \;\; 2\pi \mp 6 \frac{n_\tau}{n_e} \imath \log_{\mp} \left(\frac{-s_l + 8 s_h \mp \imath 8 (s_l + 8 s_h) \sqrt{{}_{\pm} \, \frac{s_h}{s_l + 8 s_h}}}{s_l + 24 s_h} \right) \quad ,$$

$$\sqrt{{}_{\pm}\mathbb{A}_{\text{bdry}}} \;\; = \;\; \frac{\sqrt{3}}{4} s_l \quad ,$$

$$\delta_{\text{bdry}}^{\pm} \;\; = \;\; \pi \mp 2\imath \log_{\mp} \left(\frac{\sqrt{s_l} \mp \imath 2\sqrt{6} \sqrt{{}_{\pm} \, s_h}}{\sqrt{{}_{\pm} \, s_l + 24 s_h}} \right) \quad ,$$

$$\sqrt{{}_{\pm}\mathbb{V}_\sigma} \;\; = \;\; \frac{\sqrt{2}}{48} s_l^{3/2} \sqrt{{}_{\pm} \, s_h} \quad . \tag{A2}$$

The variable s_l gives the squared length of the edges in the boundary of the 600-cell, and s_h gives the (signed) squared height of the four-simplices, into which the 600-cell is divided.

We can replace s_l and s_h by the (signed) area squares $\mathbb{A}_{\mathrm{bdry}}$ and $\mathbb{A}_{\mathrm{blk}}$, using the relations in (A2). We then obtain the action as a function of this area (squares).

We have for the shell model

$$\pm\imath\,(8\pi G)S_{\mathrm{Shell}}^{\pm} \;=\; n_e\sqrt{\mathbb{A}_{\mathrm{blk}}}\,\delta_{\mathrm{blk}}^{\pm} + n_t\left(\sqrt{\pm\mathbb{A}_{\mathrm{bdry}_1}}\,\delta_{\mathrm{bdry}_1}^{\pm} + \sqrt{\pm\mathbb{A}_{\mathrm{bdry}_2}}\,\delta_{\mathrm{bdry}_2}^{\pm}\right) - \Lambda n_\tau\sqrt{\pm\mathbb{V}_{\text{4-frust}}}\;,\qquad\text{(A3)}$$

where we have now

$$\sqrt{\pm\mathbb{A}_{\mathrm{blk}}} \;=\; \frac{\sqrt{s_{l_1}}+\sqrt{s_{l_2}}}{4\sqrt{2}}\sqrt{\pm\left(\sqrt{s_{l_2}}-\sqrt{s_{l_1}}\right)^2+8s_h}\;,$$

$$\delta_{\mathrm{blk}}^{\pm} \;=\; 2\pi\mp 6\frac{n_\tau}{n_e}\imath\log_{\mp}\left(\frac{-\left(\sqrt{s_{l_2}}-\sqrt{s_{l_1}}\right)^2+8s_h\mp\imath 8\left(\left(\sqrt{s_{l_2}}-\sqrt{s_{l_1}}\right)^2+8s_h\right)\sqrt{\pm\frac{s_h}{\left(\sqrt{s_{l_2}}-\sqrt{s_{l_1}}\right)^2+8s_h}}}{\left(\sqrt{s_{l_2}}-\sqrt{s_{l_1}}\right)^2+24s_h}\right)\;,$$

$$\sqrt{\pm\mathbb{A}_{\mathrm{bdry}_1}} \;=\; \frac{\sqrt{3}}{4}s_{l_1}\;,\qquad \sqrt{\pm\mathbb{A}_{\mathrm{bdry}_2}} \;=\; \frac{\sqrt{3}}{4}s_{l_2}\;,$$

$$\delta_{\mathrm{bdry}_1}^{\pm} \;=\; \pi\mp 2\imath\log_{\mp}\left(\frac{\left(\sqrt{s_{l_1}}-\sqrt{s_{l_2}}\right)\mp\imath 2\sqrt{6}\sqrt{\pm s_h}}{\sqrt{\pm\left(\sqrt{s_{l_2}}-\sqrt{s_{l_1}}\right)^2+24s_h}}\right)\;,\qquad \delta_{\mathrm{bdry}_2}^{\pm} \;=\; \pi\mp 2\imath\log_{\mp}\left(\frac{\left(\sqrt{s_{l_2}}-\sqrt{s_{l_1}}\right)\mp\imath 2\sqrt{6}\sqrt{\pm s_h}}{\sqrt{\pm\left(\sqrt{s_{l_2}}-\sqrt{s_{l_1}}\right)^2+24s_h}}\right)\;,$$

$$\sqrt{\pm\mathbb{V}_{\text{4-frust}}} \;=\; \frac{\sqrt{2}}{48}\left(\sqrt{s_{l_1}}+\sqrt{s_{l_2}}\right)\left(s_{l_2}+s_{l_1}\right)\sqrt{\pm s_h}\;.\qquad\text{(A4)}$$

Here, s_{l_1} and s_{l_2} give the squared edge lengths in the inner and outer boundaries of the shell, respectively. The variable s_h is the (signed) height square in the four-dimensional frusta, which build up the shell. We can again replace these variables by the (signed) squared areas $\mathbb{A}_{\mathrm{bdry}_1}$ and $\mathbb{A}_{\mathrm{bdry}_2}$ as well as $\mathbb{A}_{\mathrm{blk}}$.

Notes

[1]   Ref. [40] considers the amplitude for a four-simplex and [41] applies a refining 1-4 Pachner move to each of the five boundary tetrahedra of the four-simplex. This does lead to five bulk tetrahedra but no bulk triangles.

[2]   The smaller the parameter, the stronger the suppression.

[3]   Recent work [53,54] has, however, shown that the continuum limit of the (linearized) Area Regge dynamics leads to (linearized) general relativity, with a correction (second order in the lattice constant) given by the square of the Weyl curvature.

[4]   These frusta can be subdivided into 4-simplices, but this introduces additional edge lengths. In this model, we fix these additional edge lengths by demanding that the frusta are piecewise flat building blocks [48]. Frusta, which, however, have a cubic instead of a tetrahedral base, have also been used in [84] in the context of restricted spin foam models.

[5]   In [85,86], these are dubbed local causality condition. However, one can argue that, even to points violating these conditions, one can assign a well-defined future and past. We thus prefer the notion of irregular light cone structure.

[6]   In case the triangulation has a boundary, one has a (Gibbons–Hawking–York) boundary term [89]. This boundary term has the same structure as the bulk term; the only difference is that the deficit angles are replaced by extrinsic curvature angles. The latter are computed in the same way as the deficit angles; one only needs to replace the flat angle with the flat half-angle, or some other choice if one considers corners.

[7]   See [23] for an extensive discussion on the analytical continuation of this action and the resulting Riemann surface.

[8]   In the continuum model, one finds two Euclidean critical values for a positive imaginary lapse. These two values correspond to an evolution that remains in one hemisphere of the de Sitter sphere and an evolution that crosses the equator and therefore involves both hemispheres. Using only one time step in the discrete model, we only see the first case; to see the second solution, one needs at least two time steps.

[9]   In the continuum, one again finds two solutions corresponding to the solution not crossing or crossing the equator of the Lorentzian de Sitter space. Discretely (with only one time step), we only find the solution that does not cross the equator.

[10] One actually has $\mathbb{A}_{\mathrm{space-like}} = \ell_{\mathrm{Planck}}^4\gamma^2 j(j+1)$ only for space-like areas in a space-like tetrahedron. For space-like areas in a time-like tetrahedron, one rather has $\mathbb{A}_{\mathrm{space-like}} = \ell_{\mathrm{Planck}}^4\gamma^2 j(j-1)$ and the condition $j\geq 1$ [43]. The equidistant spectrum is a compromise, where we do not need to distinguish between these two types of space-like areas.

[11] We observed that an action that asymptotes to a quadratic growth in the summation variable might be harder to treat. The reasons are pseudo saddle points, which can appear because of the interplay between the frequency of the oscillations in the amplitude and the discretization of the variable, which defines the density with which the amplitude is probed. See Figure 12 for an example of a pseudo saddle point. With a quadratic growth of the action in the summation variable, such pseudo saddle points

will appear and can lead to the partial sums exhibiting a staircase like behavior, that is, oscillating around one value for a certain range of the cut-off, but then suddenly changing to oscillations around another value if this cut-off crosses a threshold value corresponding to a pseudo saddle point. Such a behavior is not well approximated by series of the form (16), and Wynn's epsilon algorithm has to be expected to fail in capturing the infinite sum.

[12] The path integral includes a priori integrals over the scale factors at each time step and over a lapse at each time step. After a variable transformation, the action can be made to be quadratic in a variable related to the scale factors, and this variable can be integrated out. The lapse variables are gauge-fixed, leaving only a global lapse parameter to be integrated over.

[13] The discrete analytical continuation can be uniquely specified if one provides the function values for positive real integers and positive imaginary integers. Trying different choices for the values of the function for positive imaginary integers, we always found directions in the positive complex half-plane in which the discrete analytical continuation diverges.

[14] In the plots, we translate again the boundary areas to scale factors squared by comparing the three volumes in the simplicial model with the three volumes of the spatial hypersurfaces in the mini-superspace model (see [48]).

[15] There is no classical solution, but we do have a saddle point along Euclidean data. We refer to the position of this saddle point as "classical value".

[16] See Note 11.

[17] See Note 11.

[18] In contrast, the works [34,38,39], which aimed to extract cosmological dynamics from the EPRL model [5,6], had to focus on this question and did not include a (lapse-like) bulk variable.

[19] Here, we find that the cases with Euclidean critical points lead to an exponentially suppressed amplitude (consistent with [8,23]). Note that we decided to sum over the hinge irregular configurations with a choice of (complex) Regge action, leading to exponentially suppressed amplitudes. We expect to find a different result if we implement the opposite choice. Finding an exponentially suppressed amplitude is compatible with the findings of [105], which apply a saddle point approximation for the one-simplex amplitude expressed as an integral over continuous parameters. On the other hand, [40] does find a non-suppressed amplitude for a discretization given by one (not further subdivided) simplex. The reason is the so-called vector geometries, which are thought to describe degenerate configurations [106]. It is still open whether such vector geometries should be allowed in the spin foam path, integral or not [107].

References

1. de Boer, J.; Dittrich, B.; Eichhorn, A.; Giddings, S.B.; Gielen, S.; Liberati, S.; Livine, E.R.; Oriti, D.; Papadodimas, K.; Pereira, A.D.; et al. Frontiers of Quantum Gravity: Shared challenges, converging directions. *arXiv* **2022**, arXiv:2207.10618.
2. Ambjorn, J.; Loll, R. Nonperturbative Lorentzian quantum gravity, causality and topology change. *Nucl. Phys. B* **1998**, *536*, 407–434. [CrossRef]
3. Ambjorn, J.; Jurkiewicz, J.; Loll, R. A Nonperturbative Lorentzian path integral for gravity. *Phys. Rev. Lett.* **2000**, *85*, 924–927. [CrossRef] [PubMed]
4. Ambjorn, J.; Jurkiewicz, J.; Loll, R. Dynamically triangulating Lorentzian quantum gravity. *Nucl. Phys. B* **2001**, *610*, 347–382. [CrossRef]
5. Engle, J.; Livine, E.; Pereira, R.; Rovelli, C., LQG vertex with finite Immirzi parameter. *Nucl. Phys. B* **2008**, *799*, 136. [CrossRef]
6. Freidel, L.; Krasnov, K. A New Spin Foam Model for 4d Gravity. *Class. Quant. Grav.* **2008**, *25*, 125018. [CrossRef]
7. Perez, A. The Spin Foam Approach to Quantum Gravity. *Living Rev. Rel.* **2013**, *16*, 3. [CrossRef] [PubMed]
8. Feldbrugge, J.; Lehners, J.L.; Turok, N. Lorentzian quantum cosmology. *Phys. Rev. D* **2017**, *95*, 103508. [CrossRef]
9. Asante, S.K.; Dittrich, B.; Padua-Arg uelles, J. Effective spin foam models for Lorentzian quantum gravity. *Class. Quant. Grav.* 2021, *in press*. [CrossRef]
10. Ito, Y.; Kadoh, D.; Sato, Y. Tensor network approach to 2D Lorentzian quantum Regge calculus. *Phys. Rev. D* **2022**, *106*, 106004. [CrossRef]
11. Gibbons, G.W.; Hawking, S.W.; Perry, M.J. Path Integrals and the Indefiniteness of the Gravitational Action. *Nucl. Phys. B* **1978**, *138*, 141–150. [CrossRef]
12. Lefschetz, S. Applications of Algebraic Topology, Graphs and Networks, the Picard-Lefschetz Theory and Feynman Integrals ; Applied Mathematical Sciences; Springer: Berlin, Germany; New York, NY, USA, 1975; Volume 16.
13. Vassiliev, V.A. *Applied Picard-Lefschetz Theory*; Mathematical Surveys and Monographs; AMS: Providence, RI, USA, 2002; Volume 97.
14. Witten, E. Analytic Continuation Of Chern-Simons Theory. *AMS/IP Stud. Adv. Math.* **2011**, *50*, 347–446.
15. Witten, E. A New Look At The Path Integral Of Quantum Mechanics. *arXiv* **2010**, arXiv:1009.6032.
16. Tanizaki, Y.; Koike, T. Real-time Feynman path integral with Picard–Lefschetz theory and its applications to quantum tunneling. *Annals Phys.* **2014**, *351*, 250–274. [CrossRef]
17. Cristoforetti, M.; Di Renzo, F.; Scorzato, L.; AuroraScience Collaboration. New approach to the sign problem in quantum field theories: High density QCD on a Lefschetz thimble. *Phys. Rev. D* **2012**, *86*, 074506. [CrossRef]
18. Bongiovanni, L. Numerical methods for the sign problem in Lattice Field Theory. *arXiv* **2016**, arXiv:1603.06458.

19. Alexandru, A.; Basar, G.; Bedaque, P.F.; Warrington, N.C. Complex Paths Around The Sign Problem. *Rev. Mod. Phys.* **2022**, *94*, 015006. [CrossRef]
20. Fujisawa, G.; Nishimura, J.; Sakai, K.; Yosprakob, A. Backpropagating Hybrid Monte Carlo algorithm for fast Lefschetz thimble calculations. *arXiv* **2022**, arXiv:2112.10519.
21. Han, M.; Huang, Z.; Liu, H.; Qu, D.; Wan, Y. Spinfoam on a Lefschetz thimble: Markov chain Monte Carlo computation of a Lorentzian spinfoam propagator. *Phys. Rev. D* **2021**, *103*, 084026. [CrossRef]
22. Jia, D. Complex, Lorentzian, and Euclidean simplicial quantum gravity: Numerical methods and physical prospects. *Class. Quantum Gravity* **2022**, *39*, 065002. [CrossRef]
23. Asante, S.K.; Dittrich, B.; Padua-Arg uelles, J. Complex actions and causality violations: Applications to Lorentzian quantum cosmology. *Class. Quantum Gravity* **2023**, *40*, 105005. [CrossRef]
24. Rovelli, C. *Quantum Gravity*; Cambridge University Press: Cambridge, UK, 2004 . [CrossRef]
25. Thiemann, T. *Modern Canonical Quantum General Relativity*; Cambridge University Press: Cambridge, UK, 2007. . 10.1017/CBO9780511755682. [CrossRef]
26. Bojowald, M. Loop quantum cosmology. *Living Rev. Relativ.* **2005**, *8*, 11. [CrossRef] [PubMed]
27. Ashtekar, A.; Singh, P. Loop Quantum Cosmology: A Status Report. *Class. Quantum Gravity* **2011**, *28*, 213001. [CrossRef]
28. Banerjee, K.; Calcagni, G.; Martin-Benito, M. Introduction to loop quantum cosmology. *SIGMA* **2012**, *8*, 016. [CrossRef]
29. Agullo, I.; Singh, P. Loop Quantum Cosmology. *Living Rev. Relativ.* **2008**, *11*, 1–131.
30. Bojowald, M. Critical evaluation of common claims in loop quantum cosmology. *Universe* **2020**, *6*, 36. [CrossRef]
31. Bojowald, M. Noncovariance of "covariant polymerization" in models of loop quantum gravity. *Phys. Rev. D* **2021**, *103*, 126025. [CrossRef]
32. Brunnemann, J.; Fleischhack, C. On the configuration spaces of homogeneous loop quantum cosmology and loop quantum gravity. *arXiv* **2007**, arXiv:0709.1621.
33. Brunnemann, J.; Koslowski, T.A. Symmetry Reduction of Loop Quantum Gravity. *Class. Quantum Gravity* **2011**, *28*, 245014. [CrossRef]
34. Bianchi, E.; Rovelli, C.; Vidotto, F. Towards Spinfoam Cosmology. *Phys. Rev. D* **2010**, *82*, 084035. [CrossRef]
35. Dona, P.; Frisoni, P. How-to Compute EPRL Spin Foam Amplitudes. *Universe* **2022**, *8*, 208. [CrossRef]
36. Asante, S.K.; Dittrich, B.; Haggard, H.M. Effective Spin Foam Models for Four-Dimensional Quantum Gravity. *Phys. Rev. Lett.* **2020**, *125*, 231301. [CrossRef] [PubMed]
37. Asante, S.K.; Dittrich, B.; Haggard, H.M. Discrete gravity dynamics from effective spin foams. *Class. Quantum Gravity* **2021**, *38*, 145023. [CrossRef]
38. Bianchi, E.; Krajewski, T.; Rovelli, C.; Vidotto, F. Cosmological constant in spinfoam cosmology. *Phys. Rev. D* **2011**, *83*, 104015. [CrossRef]
39. Vidotto, F. Many-nodes/many-links spinfoam: The homogeneous and isotropic case. *Class. Quantum Gravity* **2011**, *28*, 245005. [CrossRef]
40. Gozzini, F.; Vidotto, F. Primordial Fluctuations From Quantum Gravity. *Front. Astron. Space Sci.* **2021**, *7*, 629466. [CrossRef]
41. Frisoni, P.; Gozzini, F.; Vidotto, F. Markov chain Monte Carlo methods for graph refinement in spinfoam cosmology. *Class. Quantum Gravity* **2023**, *40*, 105001. [CrossRef]
42. Weniger, E.J. Nonlinear sequence transformations for the acceleration of convergence and the summation of divergent series. *Comput. Phys. Rep.* **1989**, *10*, 189. [CrossRef]
43. Conrady, F.; Hnybida, J. A spin foam model for general Lorentzian 4-geometries. *Class. Quantum Gravity* **2010**, *27*, 185011. [CrossRef]
44. Rovelli, C.; Smolin, L. Discreteness of area and volume in quantum gravity. *Nucl. Phys. B* **1995**, *442*, 593–622; Erratum in *Nucl. Phys. B* **1995**, *456*, 753–754. [CrossRef]
45. Ashtekar, A.; Lewandowski, J. Quantum theory of geometry. 1: Area operators. *Class. Quantum Gravity* **1997**, *14*, A55–A82. [CrossRef]
46. Gielen, S.; Oriti, D.; Sindoni, L. Cosmology from Group Field Theory Formalism for Quantum Gravity. *Phys. Rev. Lett.* **2013**, *111*, 031301. [CrossRef]
47. Gielen, S.; Oriti, D.; Sindoni, L. Homogeneous cosmologies as group field theory condensates. *J. High Energy Phys.* **2014**, *6*, 013. [CrossRef]
48. Dittrich, B.; Gielen, S.; Schander, S. Lorentzian quantum cosmology goes simplicial. *Class. Quantum Gravity* **2022**, *39*, 035012. [CrossRef]
49. Regge, T. General Relativity Without Coordinates. *Nuovo Cim.* **1961**, *19*, 558. [CrossRef]
50. Dittrich, B.; Ryan, J.P. Phase space descriptions for simplicial 4d geometries. *Class. Quantum Gravity* **2011**, *28*, 065006. [CrossRef]
51. Dittrich, B.; Ryan, J.P. Simplicity in simplicial phase space. *Phys. Rev. D* **2010**, *82*, 064026. [CrossRef]
52. Dittrich, B.; Ryan, J.P. On the role of the Barbero-Immirzi parameter in discrete quantum gravity. *Class. Quantum Gravity* **2013**, *30*, 095015. [CrossRef]
53. Dittrich, B. Modified Graviton Dynamics From Spin Foams: The Area Regge Action. *arXiv* **2021**, arXiv:2105.10808.
54. Dittrich, B.; Kogios, A. From spin foams to area metric dynamics to gravitons. *Class. Quantum Gravity* **2023**, *40*, 095011. [CrossRef]

55. Borissova, J.N.; Dittrich, B. Towards effective actions for the continuum limit of spin foams. *Class. Quantum Gravity* **2023**, *40*, 105006. [CrossRef]
56. Dittrich, B.; Padua-Arg uelles, J. Twisted geometries are area-metric geometries. *arXiv* **2023**, arXiv:2302.11586.
57. Dittrich, B.; Speziale, S. Area-angle variables for general relativity. *New J. Phys.* **2008**, *10*, 083006. [CrossRef]
58. Asante, S.K.; Simão, J.D.; Steinhaus, S. Spin-foams as semiclassical vertices: Gluing constraints and a hybrid algorithm. *Phys. Rev. D* **2023**, *107*, 046002. [CrossRef]
59. Han, M.; Liu, H.; Qu, D. Complex critical points in Lorentzian spinfoam quantum gravity: 4-simplex amplitude and effective dynamics on double-Δ_3 complex. *arXiv* **2023**, arXiv:2301.02930.
60. Asante, S.K.; Dittrich, B.; Girelli, F.; Riello, A.; Tsimiklis, P. Quantum geometry from higher gauge theory. *Class. Quantum Gravity* **2020**, *37*, 205001. [CrossRef]
61. Baratin, A.; Freidel, L. Hidden Quantum Gravity in 4-D Feynman diagrams: Emergence of spin foams. *Class. Quantum Gravity* **2007**, *24*, 2027–2060. [CrossRef]
62. Baratin, A.; Freidel, L. A 2-categorical state sum model. *J. Math. Phys.* **2015**, *56*, 011705. [CrossRef]
63. Simão, J.D.; Steinhaus, S. Asymptotic analysis of spin-foams with timelike faces in a new parametrization. *Phys. Rev. D* **2021**, *104*, 126001. [CrossRef]
64. Dona, P.; Han, M.; Liu, H. Spinfoams and high performance computing. *arXiv* **2022**, arXiv:2212.14396.
65. Barrett, J.W.; Rocek, M.; Williams, R.M. A Note on area variables in Regge calculus. *Class. Quant. Grav.* **1999**, *16*, 1373. [CrossRef]
66. Asante, S.K.; Dittrich, B.; Haggard, H.M. The Degrees of Freedom of Area Regge Calculus: Dynamics, Non-metricity, and Broken Diffeomorphisms. *Class. Quantum Gravity* **2018**, *35*, 135009. [CrossRef]
67. Bahr, B.; Rabuffo, G.; Steinhaus, S. Renormalization of symmetry restricted spin foam models with curvature in the asymptotic regime. *Phys. Rev. D* **2018**, *98*, 106026. [CrossRef]
68. Bahr, B.; Dittrich, B. Regge calculus from a new angle. *New J. Phys.* **2010**, *12*, 033010. [CrossRef]
69. Fairbairn, W.J.; Meusburger, C. Quantum deformation of two four-dimensional spin foam models. *J. Math. Phys.* **2012**, *53*, 022501. [CrossRef]
70. Dupuis, M.; Girelli, F. Observables in Loop Quantum Gravity with a cosmological constant. *Phys. Rev. D* **2014**, *90*, 104037. [CrossRef]
71. Haggard, H.M.; Han, M.; Kamiński, W.; Riello, A. SL(2,C) Chern–Simons theory, a non-planar graph operator, and 4D quantum gravity with a cosmological constant: Semiclassical geometry. *Nucl. Phys. B* **2015**, *900*, 1–79. [CrossRef]
72. Dittrich, B. (3 + 1)-dimensional topological phases and self-dual quantum geometries encoded on Heegaard surfaces. *J. High Energy Phys.* **2017**, *5*, 123. [CrossRef]
73. Han, M. Four-dimensional spinfoam quantum gravity with a cosmological constant: Finiteness and semiclassical limit. *Phys. Rev. D* **2021**, *104*, 104035. [CrossRef]
74. Bahr, B.; Dittrich, B. Improved and Perfect Actions in Discrete Gravity. *Phys. Rev. D* **2009**, *80*, 124030. [CrossRef]
75. Breaking and restoring of diffeomorphism symmetry in discrete gravity. *AIP Conf. Proc.* **2009**, *1196*, 10.
76. Asante, S.K.; Dittrich, B.; Steinhaus, S. Spin foams, Refinement limit and Renormalization. *arXiv* **2022**, arXiv:2211.09578.
77. Dittrich, B. Diffeomorphism symmetry in quantum gravity models. *Adv. Sci. Lett.* **2009**, *2*, 151. [CrossRef]
78. Bahr, B.; Dittrich, B. (Broken) Gauge Symmetries and Constraints in Regge Calculus. *Class. Quantum Gravity* **2009**, *26*, 225011. [CrossRef]
79. Hartle, J.B. Simplicial minisuperspace I. General discussion. *J. Math. Phys.* **1985**, *26*, 804–814. [CrossRef]
80. Hartle, J.B. Simplicial minisuperspace. II. Some classical solutions on simple triangulations. *J. Math. Phys.* **1986**, *27*, 287–295. [CrossRef]
81. Hartle, J.B. Simplicial minisuperspace. III. Integration contours in a five-simplex model. *J. Math. Phys.* **1989**, *30*, 452–460. [CrossRef]
82. Collins, P.A.; Williams, R.M. Dynamics of the Friedmann Universe Using Regge Calculus. *Phys. Rev. D* **1973**, *7*, 965–971. [CrossRef]
83. Liu, R.G.; Williams, R.M. Regge calculus models of the closed vacuum Λ–FLRW universe. *Phys. Rev. D* **2016**, *93*, 024032. [CrossRef]
84. Bahr, B.; Kloser, S.; Rabuffo, G. Towards a Cosmological subsector of Spin Foam Quantum Gravity. *Phys. Rev. D* **2017**, *96*, 086009. [CrossRef]
85. Jordan, S.; Loll, R. Causal Dynamical Triangulations without Preferred Foliation. *Phys. Lett. B* **2013**, *724*, 155–159. [CrossRef]
86. Jordan, S.; Loll, R. De Sitter Universe from Causal Dynamical Triangulations without Preferred Foliation. *Phys. Rev. D* **2013**, *88*, 044055. [CrossRef]
87. Sorkin, R. Time Evolution Problem in Regge Calculus. *Phys. Rev. D* **1975**, *12*, 385–396; Erratum in *Phys. Rev. D* **1981**, *23*, 565–565. [CrossRef]
88. Sorkin, R.D. Lorentzian angles and trigonometry including lightlike vectors. *arXiv* **2019**, arXiv:1908.10022.
89. Hartle, J.B.; Sorkin, R. Boundary Terms in the Action for the Regge Calculus. *Gen. Rel. Grav.* **1981**, *13*, 541–549. [CrossRef]
90. Dittrich, B.; Jacobson, T.; Padua-Arg uelles, J. De Sitter horizon entropy from a simplicial Lorentzian path integral. *arXiv* **2024**, arXiv:2403.02119.
91. Dorronsoro, J.D.; Halliwell, J.J.; Hartle, J.B.; Hertog, T.; Janssen, O. Real no-boundary wave function in Lorentzian quantum cosmology. *Phys. Rev. D* **2017**, *96*, 043505. [CrossRef]
92. Bojowald, M. Loop quantum cosmology. *Living Rev. Rel.* **2008**, *11*, 4. [CrossRef] [PubMed]

93. Ashtekar, A.; Pawlowski, T.; Singh, P. Quantum Nature of the Big Bang: Improved dynamics. *Phys. Rev. D* **2006**, *74*, 084003. [CrossRef]
94. Beetle, C.; Engle, J.S.; Hogan, M.E.; Mendonça, P. Diffeomorphism invariant cosmological sector in loop quantum gravity. *Class. Quantum Gravity* **2017**, *34*, 225009. [CrossRef]
95. Schmidt, J.R. On the numerical solution of linear simultaneous equations by an iterative method. *Philos. Mag.* **1941**, *32*, 369. [CrossRef]
96. Shanks, D. Non-linear transformations of divergent and slowly convergent sequences. *J. Math. Phys.* **1955**, *34*, 1. [CrossRef]
97. Wynn, P. On a device for computing the $e_m(S_n)$ transformation. *Math. Tables Aids Comput.* **1956**, *10*, 91. [CrossRef]
98. Wynn, P. A note on programming repeated applications of the ϵ-algorithm. *R.F.T.I.—Chiffres* **1965**, *8*, 23.
99. Aitken, A. On Bernoulli's Numerical Solution of Algebraic Equations. *Proc. R. Soc. Edinb.* **1927**, *46*, 289–305. [CrossRef]
100. Donà, P.; Frisoni, P. Summing bulk quantum numbers with Monte Carlo in spin foam theories. *Phys. Rev. D* **2023**, *107*, 106008. [CrossRef]
101. Hartle, J.B.; Hawking, S.W. Wave Function of the Universe. *Phys. Rev. D* **1983**, *28*, 2960–2975. [CrossRef]
102. Duffin, R.J. Basic properties of discrete analytic functions. *Duke Math. J.* **1956**, *23*, 335. [CrossRef]
103. Borissova, J.; Dittrich, B.; Qu, D.; Schiffer, M. Spikes and spines in 3D Lorentzian simplicial quantum gravity. *arXiv* **2024**, arXiv:2406.19169.
104. Borissova, J.; Dittrich, B.; Qu, D.; Schiffer, M. Spikes and spines in 4D Lorentzian simplicial quantum gravity. *arXiv* **2024**, *to appear*
105. Han, M.; Liu, H. Analytic Continuation of Spin foam Models. *arXiv* **2021**, arXiv:2104.06902.
106. Barrett, J.W.; Dowdall, R.J.; Fairbairn, W.J.; Hellmann, F.; Pereira, R. Lorentzian spin foam amplitudes: Graphical calculus and asymptotics. *Class. Quantum Gravity* **2010**, *27*, 165009. [CrossRef]
107. Engle, J. A spin-foam vertex amplitude with the correct semiclassical limit. *Phys. Lett. B* **2013**, *724*, 333–337. [CrossRef]
108. Dittrich, B. From the discrete to the continuous: Towards a cylindrically consistent dynamics. *New J. Phys.* **2012**, *14*, 123004. [CrossRef]
109. Dittrich, B. The continuum limit of loop quantum gravity—A framework for solving the theory. *arXiv* **2014**, arXiv:1409.1450.
110. Bahr, B.; Dittrich, B.; Steinhaus, S. Perfect discretization of reparametrization invariant path integrals. *Phys. Rev. D* **2011**, *83*, 105026. [CrossRef]
111. Dittrich, B.; Steinhaus, S. Path integral measure and triangulation independence in discrete gravity. *Phys. Rev. D* **2012**, *85*, 044032. [CrossRef]
112. Borissova, J.N.; Dittrich, B. Lorentzian quantum gravity via Pachner moves: One-loop evaluation. *arXiv* **2023**, arXiv:2303.07367.
113. Dittrich, B.; Hohn, P.A. From covariant to canonical formulations of discrete gravity. *Class. Quantum Gravity* **2010**, *27*, 155001. [CrossRef]
114. Dittrich, B.; Hoehn, P.A. Constraint analysis for variational discrete systems. *J. Math. Phys.* **2013**, *54*, 093505. [CrossRef]
115. Dittrich, B.; Padua-Argüelles, J. Bianchi I quantum cosmology from effective spin foams. *arXiv* **2023**, *to appear*.
116. Genz, A.C. A nonlinear method for the acceleration of the convergence of multidimensional squences. *J. Comput. Appl. Math.* **1977**, *3*, 181. [CrossRef]